National Laser Users' Facility and External Users' Programs

During FY07, 826 target shots were taken on OMEGA for external users' experiments, accounting for 54.6% of the total OMEGA shots for the year. The external users during this year included six collaborative teams participating in the National Laser Users' Facility (NLUF) program and many collaborative teams from the national laboratories (LLNL, LANL, and SNL), the Commissariat à l'Énergie Atomique (CEA) of France, and the Atomic Weapons Establishment (AWE) of the United Kingdom.

FY07 NLUF Experiments

FY07 was the first of a two-year period of performance for the NLUF projects approved for the FY07–FY08 funding and OMEGA shots (see Table 112.VI). Six of these NLUF projects were allotted OMEGA shot time and received a total of 131 shots on OMEGA in FY07. Some of this work is summarized in this section.

Recreating Planetary Core States on OMEGA in FY07

Principal Investigator: R. Jeanloz (University of California, Berkeley)

Co-investigators: J. H. Eggert, P. M. Celliers, S. Brygoo, D. G. Hicks, and G. W. Collins (LLNL); P. Loubeyre (CEA); T. R. Boehly (LLE); S. McWilliams and D. Spaulding (U.C. Berkeley)

The approach to recreate planetary core states in the laboratory involves driving a laser-induced shock through a sample already precompressed in a diamond-anvil cell (Fig. 112.40). This combines the benefits of static and dynamic high-pressure experiments, allowing the final pressure–volume–temperature (P–V–T) state of the sample to be tuned across a broad range of thermodynamic conditions. Much higher densities are achieved through this approach than through traditional shock-wave

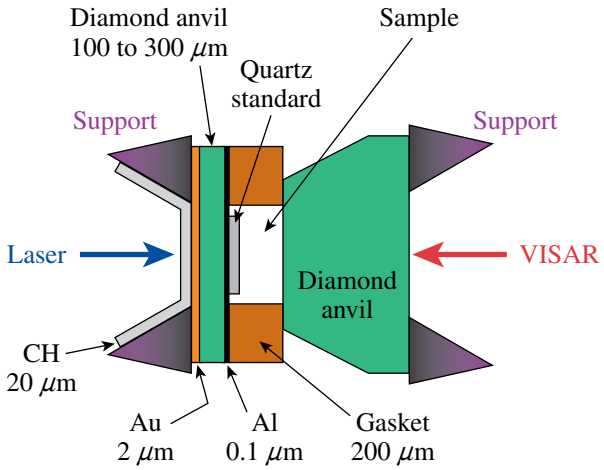

Figure 112.40
Schematic cross section of the diamond cell. The diamond anvil on the entry (drive laser) side must be thin in order to minimize attenuation of the shock front before it enters the sample, and diagnostics include velocity interferometry system for any reflector (VISAR) as well as pyrometry (not shown) collected through the thicker anvil on the exit side.

Table 112.VI: FY07–FY08 NLUF Experiments.

Principal Investigator	Affiliation	Proposal Title
R. Jeanloz	University of California, Berkeley	Recreating Planetary Core States on OMEGA in FY07
R. P. Drake	University of Michigan	Experimental Astrophysics on the OMEGA Laser
P. Hartigan	Rice University	Laboratory Experiments on Supersonic Astrophysical Flows Interacting with Clumpy Environments
R. Mancini	University of Nevada, Reno	Multiview Tomographic Study of OMEGA Direct-Drive-Implosion Experiments
R. D. Petrasso, C. K. Li	Massachusetts Institute of Technology	Monoenergetic Proton Radiography of Laser–Plasma-Generated Fields and ICF Implosions
R. Falcone, H. J. Lee	University of California, Berkeley	X-Ray Compton Scattering on Compressed Matter

(Hugoniot) measurements because thermal effects come to dominate the latter but are suppressed by the precompression.

Thus, states directly relevant to the deep interiors of giant planets are reproduced, and we can study interatomic-bonding forces at much closer packing than is otherwise possible through laboratory experiments. This is important both for planetary science and for validating (and extending) the condensed-matter theory based on first-principles quantum-mechanical calculations.

This year we developed a technique that uses quartz as a reference standard for Hugoniot, temperature, and reflectivity measurements of planetary fluids.[1] This new technique greatly reduces the uncertainty of shock-compression data, and measurements were completed for He.[2] This work establishes how the compressibility changes with ionization and interparticle interaction and will serve as a key benchmark for models of the evolution and structure of solar and extra-solar giant planets. Temperature and reflectivity measurements on He were also finished this year, and we have collected the highest-density and pressure data for He.[3]

In addition to He, we have finished collecting shocked precompressed data on H_2 and D_2. While the deuterium data (for samples that start at the same density as liquid deuterium), have the same compressibility as impedance-matched liquid deuterium, contrasting H_2 and D_2 measurements reveals an interesting isotope dependence for the compressibility. In essence, the hydrogen shows a larger compressibility than deuterium at the same precompressed pressure. This is likely because the compressibility is sensitive to the excitation of degrees of freedom that increases the compressibility and the interparticle interaction that increases pressure and reduces the compressibility. In fact, all the tabular equation-of-state (EOS) models show this signature, with the maximum compressibility decreasing with precompression (still, the final density increases with precompression). Hydrogen, which has a larger zero-point volume because of its smaller mass, behaves like deuterium, having a lower initial density.

The reflectivity and temperature data for hydrogen reveal that contours of constant reflectance are nearly parallel to the predicted plasma phase transition derived from Saumon and Chabrier[4] and from Bonev's density functional calculations[5] (Fig. 112.41).

Finally we have finished our first set of measurements on He/H_2 mixtures, finding that the temperature and optical reflectivity are between those of He and H_2. The reflectivity of He increases slowly with shock pressure as compared to H_2. At the same time, the temperature of He increases rapidly with shock pressure as compared to H_2. These two observations are related: the reason H_2 stays colder with increasing shock pressure compared to He (over the pressure range studied) is because H_2 dissociates; also, it ionizes at much lower shock pressure than He, and the dissociation and ionization (which leads to enhanced optical reflectance) lower the shock tempera-

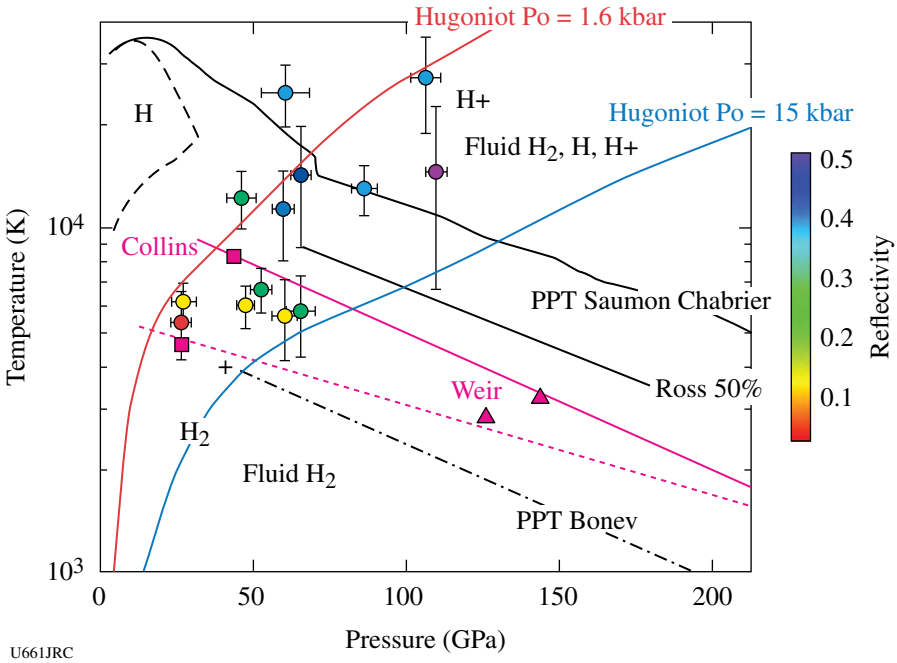

Figure 112.41
Reflectivity versus temperature and pressure for shocked precompressed H_2. Data show a continuous transition between the molecular and plasma phases in this range of temperature and pressure.

ture. Over the same pressure range (0.1 to 2 Mbar), He exhibits much lower ionization. Therefore, increasing shock pressure rapidly increases shock temperature.

The 50/50 mixture of He/H_2 shows that the temperature and shock reflectivity lie between those of H_2 and He, suggesting that the mixture can be modeled as ideal (Figs. 112.42 and 112.43).

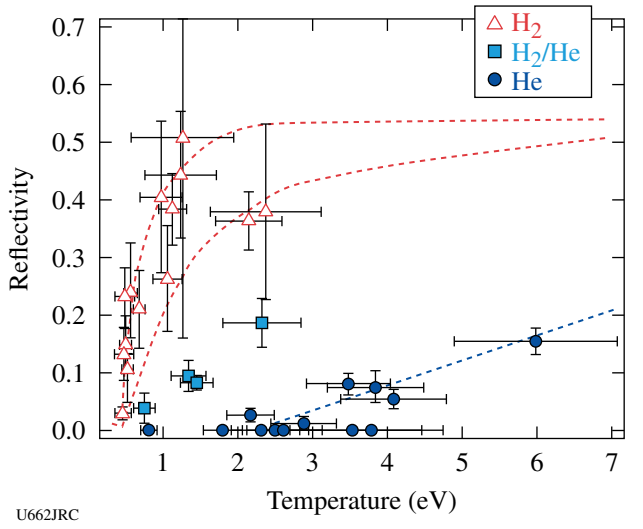

Figure 112.42
Reflectivity versus temperature for H_2, He, and a 50/50 mixture of H_2/He. These data start off at very different initial densities but, since the reflectivity is largely temperature dependent, the reflectivity for each material follows a specific trend. The reflectivity (and the temperature versus pressure) for the mixture is intermediate between that of H_2 and He.

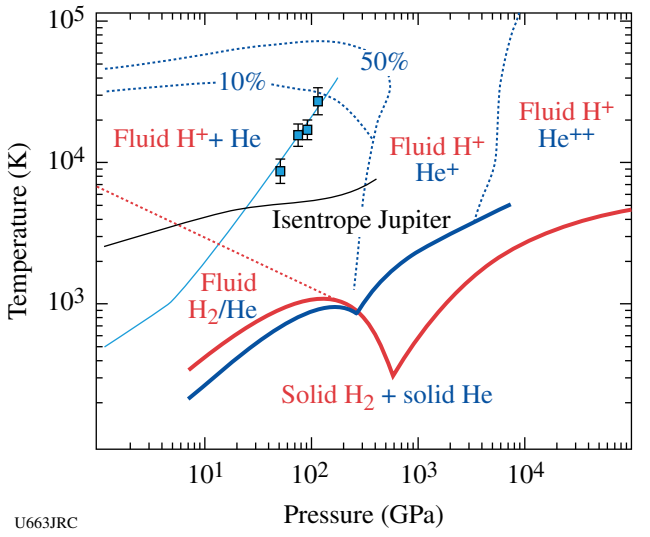

Figure 112.43
Temperature versus pressure for He/H_2. These are the first high-temperature, high-pressure data collected for this mixture that provide key information on the properties of the H_2–He mixtures dominating giant planetary interiors.

These data suggest that over the warm, dense matter states tested here, which are relevant to the outer 20% of Jupiter, the mixture does not phase separate. This is an important result, providing new constraints on models of the interior structure and evolution of giant planets. It warrants further analysis, both to refine our understanding of the experimental observations and to fully understand the implications for the evolution, therefore formation, of planets.

In summary, we completed 23 experiments in two shot days, filling out our database for H_2, He, and one mixture of He/H_2. We have characterized key properties of dense planetary fluids and have documented an interesting isotope effect in the compressibility of H_2 relative to D_2. Helium becomes electronically conducting at ~1 Mbar and 1 eV, largely by a thermally activated process. The He/H_2 mixture seems to behave like an ideal solution up to ~1 Mbar and 2 eV. Several papers are published or are in the process of publication,[1–3,6–9] and this work has ignited an explosion of papers on He, H_2, and mixtures at planetary-core conditions.

Experimental Astrophysics on the OMEGA Laser

Principal Investigator: R. P. Drake (University of Michigan)
Co-investigators: D. Arnett (University of Arizona); T. Plewa (Florida State University); A. Calder, J. Glimm, Y. Zhang, and D. Swesty (SUNY Stony Brook); M. Koenig (LULI, Ecole Polytechnique, France); C. Michaut (Observatorie de Paris, France); M. Busquet (France); J. P. Knauer and T. R. Boehly (LLE); P. Ricker (University of Illinois); B. A. Remington, H. F. Robey, J. F. Hansen, A. R. Miles, R. F. Heeter, D. H. Froula, M. J. Edwards, and S. H. Glenzer (LLNL)

The OMEGA laser is able to produce processes similar to those that occur in astrophysics because it can generate extremely high energy densities, corresponding to pressures greater than 10 Mbar in millimeter-scale targets. This project is focused on two such issues in astrophysics: the contribution of hydrodynamic instabilities to the structure in supernovae and the dynamics of radiative shock waves. To explore hydrodynamic instabilities in supernovae, it was necessary to develop new radiographic diagnostics capable of improved imaging in two orthogonal directions. We have accomplished this goal and are proceeding to study the contributions of various initial modes to the enhanced spike penetration.

In the experiment, ten OMEGA laser beams irradiate a plastic disk with UV light for 1 ns. The total energy of the beams is ~5 kJ and the average irradiance is ~9.5×10^{14} W/cm^2, producing an ablation pressure of ~50 Mbar in the plastic layer

of the target. This large pressure creates a strong shock in the plastic material, which evolves into a blast wave. The blast wave crosses a perturbed interface into a lower-density material. This process is similar to what occurs in a supernova explosion. In the experiment, we monitor the unstable evolution of the interface between the two materials using x-ray radiography.

Figure 112.44 shows data from the latest experiments to obtain physics data using simultaneous, orthogonal, point-projection backlighting. The data are obtained by using a brief (1-ns) x-ray source to project a signal onto an exposed piece of x-ray film. This experiment was imaged 21 ns after the initial laser beams had been pulsed. One can see on these images the structures that have evolved from an initial condition defined by $a_0\sin(kx)\sin(ky)$, where $a_0 = 2.5\ \mu$m and $k_x = k_y = 2\pi/(71\ \mu\text{m})$. Image (a) shows mass extensions that extend from the primary spike toward the shock. This phenomenon has not been previously observed. We have also studied the impact of a selected range of initial conditions. In the next year we plan to do an experiment that will investigate initial conditions more realistic to an actual supernova.

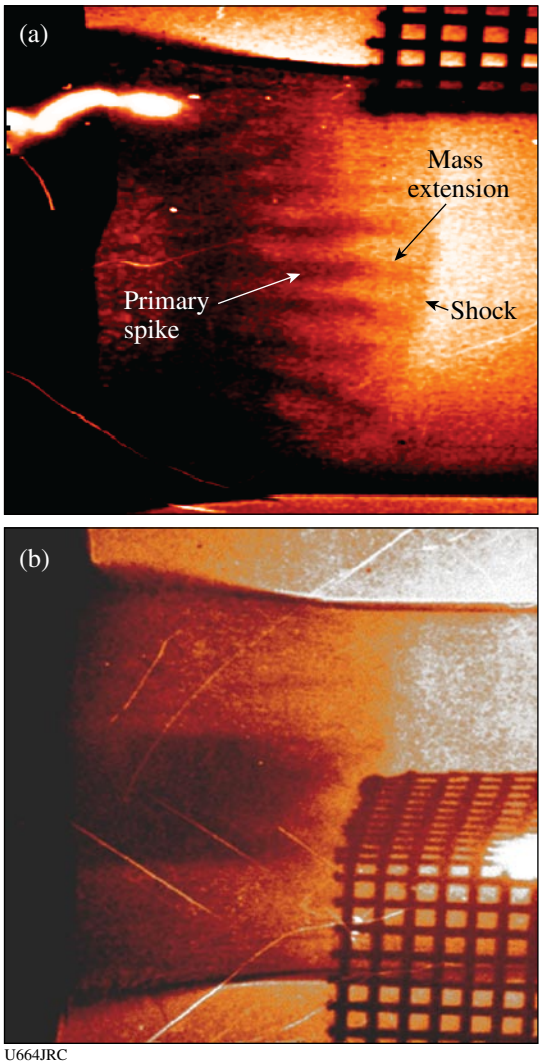

U664JRC

Figure 112.44
Simultaneous, orthogonal, point-projection x-ray backlighting images (a) and (b) of blast wave propagation in plastic material.

Laboratory Experiments on Supersonic Astrophysical Flows Interacting with Clumpy Environments

Principal Investigator: P. Hartigan (Rice University)
Co-investigators: R. Carver (Rice University); A. Frank (University of Rochester); P. A. Rosen, J. M. Foster, and R. Williams (AWE, UK); B. H. Wilde and R. Coker (LANL); B. E. Blue (LLNL)

Supersonic directed jets and outflows are important components of many astrophysical systems. Their interaction with surrounding matter results in the creation of spectacular bow shocks and the entrainment of dense clumps of interstellar material; it may also result in significant deflection of the collimated jet. The objective of this sequence of NLUF experiments is to develop a laboratory platform to study the hydrodynamics of these processes; the laboratory work is complementary to astrophysical observations using the Hubble Space Telescope (HST) and the Kitt Peak National Observatory (KPNO); furthermore, the same computer codes will be used to interpret both the laboratory and astrophysical observations.

In previous experiments on OMEGA, we have developed an experimental platform to create a dense, supersonic, titanium-plasma jet propagating through low-density foam,[10] and we have studied the deflection of this jet by a localized density perturbation.[11] During the past year, two shot days were allocated to this project: we investigated structure potentially seeded in the jet by granularity of the foam medium used in the OMEGA experiments (no significant effect was found), and we progressed further into our project by beginning our study of the interaction of a strong shock with a spherical density discontinuity in the foam. Excellent experimental data were obtained (Fig. 112.45), thereby laying the foundation for further work to study the interaction of shocks and jets with multiple clumps of material—phenomena also being observed in ongoing work using HST and KPNO. The OMEGA experiments were an important component of the case for these further astronomical observations, and our aim is to build a synergistic relationship between experiments, observation, and modeling that will provide new insight into these complex phenomena.

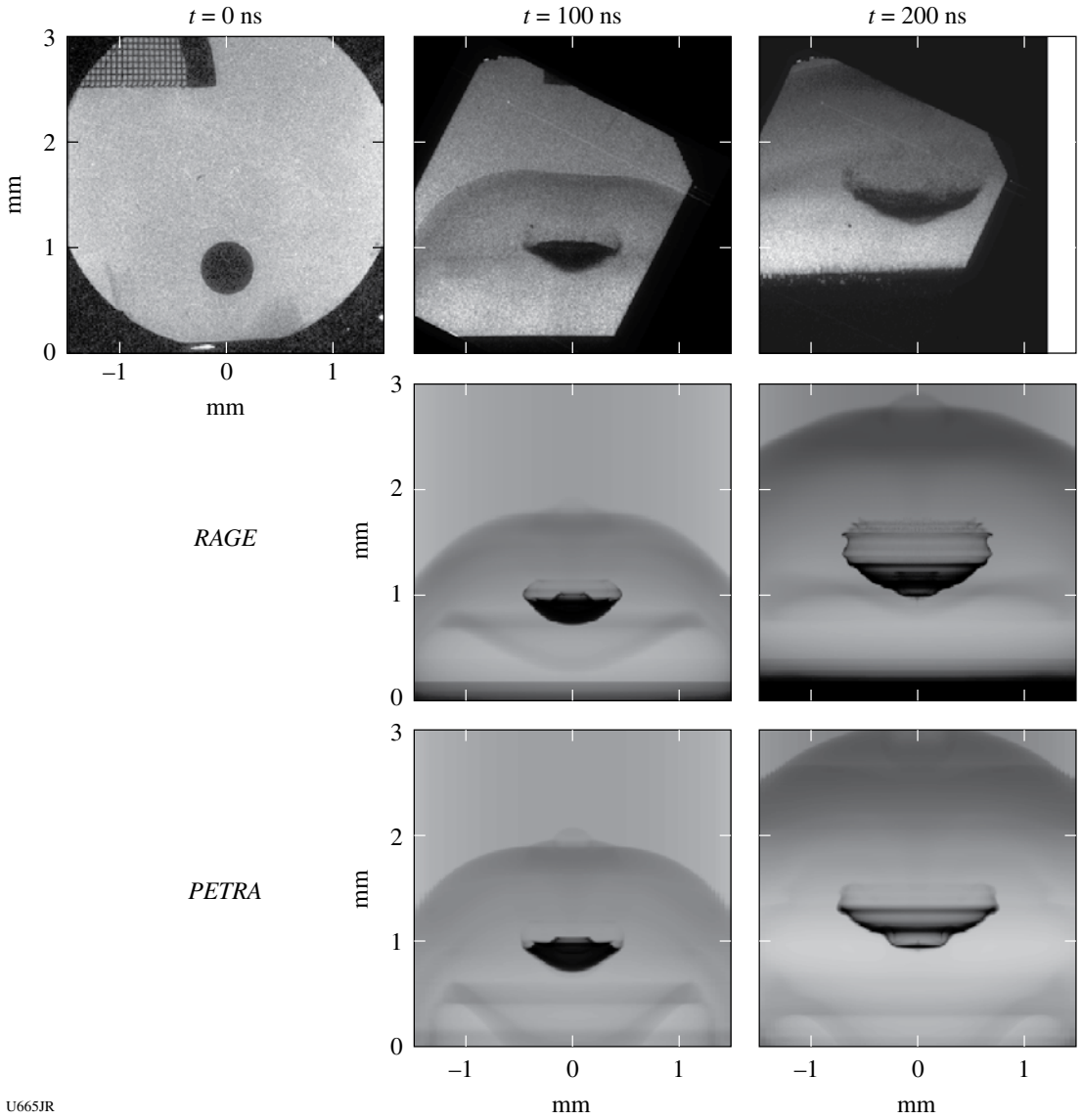

Figure 112.45
Interaction of a strong shock with a density "clump." The OMEGA laser drives a shock through hydrocarbon foam containing a 500-μm-diam sapphire sphere. The sequence of experimental images (top) at 0, 100, and 200 ns shows the shock-driven distortion and entrainment of the sphere by the hydrodynamic flow. The data are compared with modeling (center and bottom) using the *RAGE* and *PETRA* hydrocodes. These phenomena are analogous to those observed in Hubble Space Telescope images of astrophysical jets propagating through interstellar matter.

Multiview Tomographic Study of OMEGA Direct-Drive-Implosion Experiments

Principal Investigator: R. Mancini (University of Nevada, Reno)
Co-investigators: R. Tommasini, N. Izumi, and J. A. Koch (LLNL); I. E. Golovkin (PRISM); D. A. Haynes and G. A. Kyrala (LANL); J. A. Delettrez, S. P. Regan, and V. A. Smalyuk (LLE)

The determination of the spatial structure of inertial confinement fusion implosion cores is an important problem of high-energy-density physics. To this end, three identical multimonochromatic imagers (MMI's) have been designed, built, and fielded in OMEGA implosion experiments to perform observations along three quasi-orthogonal lines of sight (LOS). The implosions were driven with 60 OMEGA beams—23 kJ of UV energy in a 1-ns-duration square laser pulse; the targets were gas-filled plastic shells. At the collapse of the implosion, the hot, dense core plasma achieved temperatures in the 1- to 2-keV range and electron number densities between 1×10^{24} cm^{-3} and $2 \times$

10^{24} cm^{-3}. X-ray K-shell line emission from the argon dopant added to the fuel is a suitable spectroscopy diagnostic for this temperature and density range. In addition, x-ray absorption from a titanium tracer layer embedded in the plastic yields information about the state of the compressed shell.

Core images recorded by MMI instruments are formed by a large array of 10-μm-diam pinholes with an ~100-μm separation between pinholes and are reflected off a depth-graded WB_4C multilayer mirror with an average bilayer thickness of 15 Å. The instrument is equipped with 10-cm-long mirrors that permit the observation of narrowband x-ray images over a photon energy range from 3 to 5 keV. They have a magnification of 8.5, provide spatial resolution of approximately 10 μm, and record gated (framed) images characteristic of a 50-ps time interval. The broad photon energy range, afforded by the use of long mirrors, covers the K-shell line emission from argon ions as well as the K-shell line absorption from titanium L-shell ions. As an illustration of the data recorded by MMI's, Fig. 112.46 displays a time history (i.e., three frames) of narrowband x-ray core images from OMEGA shot 47485 recorded along one LOS at the collapse of the implosion; also shown are examples of narrowband image reconstruction from the data for several spectral features. The data effectively resolve time, space, and photon energy and show several argon line emissions, namely Ly$_\alpha$ ($1s\ ^2S$–$2p\ ^2P$, $h\nu$ = 3320 eV), He$_\alpha$ ($1s^2\ ^1S$–$1s2p\ ^1P$, $h\nu$ = 3140 eV), Ly$_\beta$ ($1s\ ^2S$–$3p\ ^2P$, $h\nu$ = 3936 eV), and He$_\beta$ ($1s^2\ ^1S$–$1s3p\ ^1P$, $h\nu$ = 3684 eV). The photon energy range of these images is given by the (mainly) Stark-broadening widths of the line shapes, which is 60 eV to 70 eV for the plasma conditions achieved in these cores. Core dimensions are in the 60- to 120-μm range. In addition, x-ray absorption in the shell due to titanium ions is also observed. These absorption features are formed by line transitions from n = 1 to n = 2 in L-shell titanium ions (e.g., F-like, O-like, etc.) in the photon energy range from 4500 to 4750 eV driven by continuum radiation emitted in the core, and their analysis permits the characterization of the compressed shell. It is interesting to observe the differences in distribution of brightness associated with the line-based core images, which depends on both temperature and density conditions in the core. Detailed spectral modeling and analysis of the emissivity and opacity of the argon x-ray

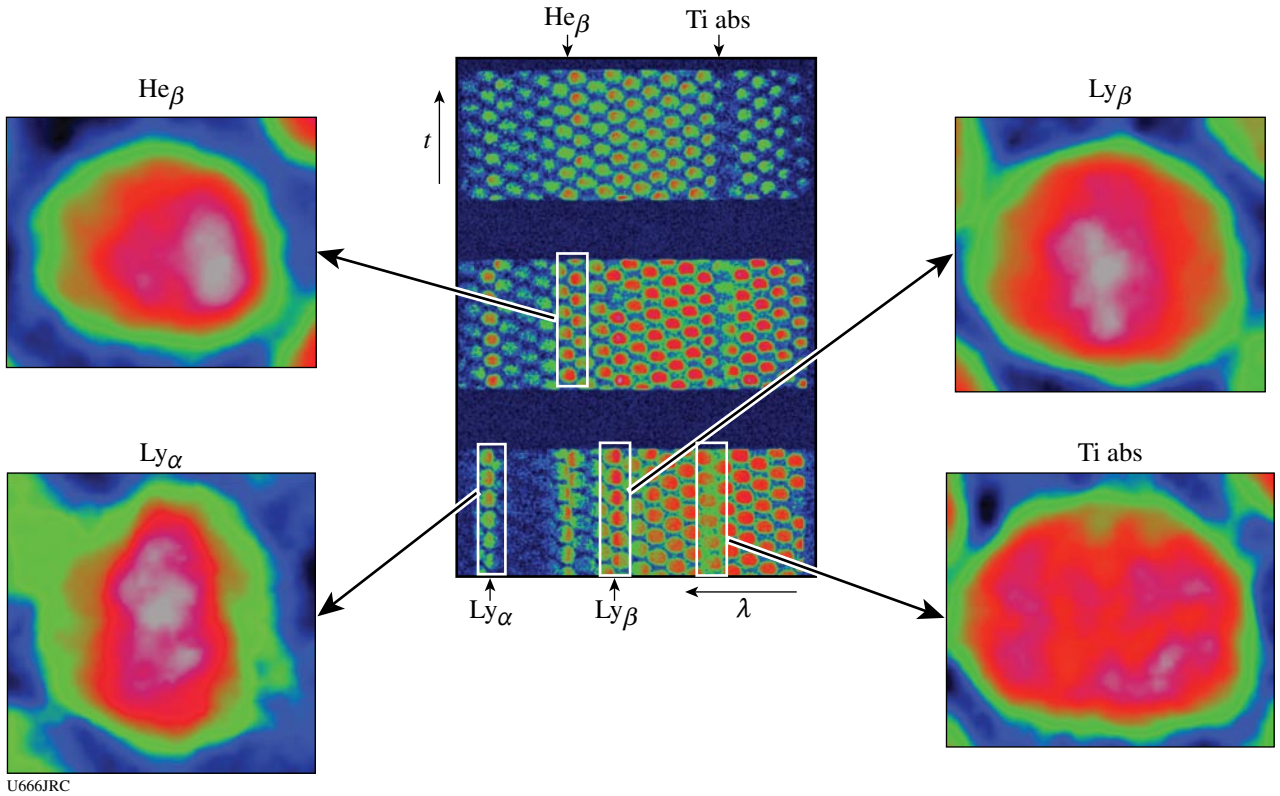

Figure 112.46
Time history (three center frames) of narrowband, x-ray core images recorded by MMI's and four narrowband image reconstructions from this data (OMEGA shot 47485).

emission permit a reconstruction of the spatial structure of the core plasma. Several analysis methods are currently being investigated that simultaneously consider data observed along several lines of sight.

Monoenergetic Proton Radiography of Laser–Plasma-Generated Fields and ICF Implosions

Principal Investigators: R. D. Petrasso and C. K. Li (Massachusetts Institute of Technology)

Co-investigators: J. A. Frenje and F. H. Séguin (MIT); J. P. Knauer and V. A. Smalyuk (LLE); R. P. J. Town (LLNL)

MIT's NLUF program has continued an ongoing series of experiments using monoenergetic charged-particle radiography to study transient electromagnetic fields generated by the interaction of OMEGA laser beams with plastic foils. This work, involving novel studies of time evolution, field instabilities, and magnetic reconnection, has resulted in the publication of three Physical Review Letters publications[12–14] and two invited talks at conferences.[15,16]

Figure 112.47 shows the basic experimental setup.[17] One or more OMEGA laser beams interact with a plastic foil, generating plasma bubbles, **B** fields, and **E** fields. A special backlighter and matched imaging detector are used to create a radiographic image of the resultant plasma/field structure. The backlighter is a glass-shell ICF capsule filled with D^3He gas and imploded by 20 OMEGA laser beams, producing D^3He protons (14.7 MeV), DD protons (3 MeV), D^3He alpha particles (3.6 MeV), and a few other fusion products. CR-39 nuclear track detectors are used in conjunction with appropriate filters and processing techniques to record individual charged particles and their energies in the detector plane. Since the burn duration of the D^3He implosion is short (~130 ps) relative to the nanosecond-scale duration of the foil illumination and subsequent evolution, and since the relative timing of the backlighter and the foil illumination was adjustable, it is possible to record images at different times relative to the foil illumination. A metal mesh is interposed between the backlighter and the foil to divide the incident particle flux into beamlets; distortion in the mesh pattern at the detector shows how the particle trajectories were deflected by the fields generated by laser–plasma interactions at the foil.

In one series of experiments (Fig. 112.48), field evolution and instabilities were studied with 14.7-MeV proton radiography when a single interaction beam was used. While the 1-ns interaction beam was on, the plasma bubble and its surrounding megagauss **B** field expanded symmetrically and roughly linearly, but then became increasingly asymmetric as expansion continued and field strength decayed. We believe this is the first direct observation and evidence of the pressure-driven, resistive-interchange instability in laser-produced high-energy-

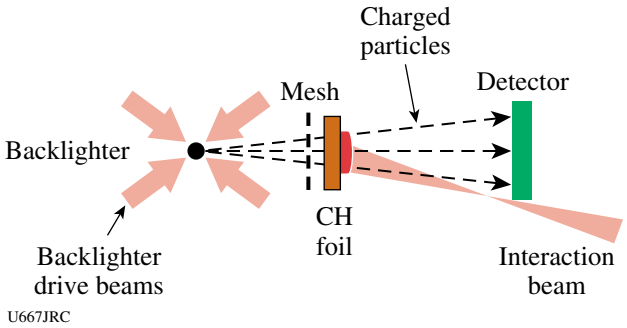

Figure 112.47
Schematic illustration of the experiment setup and the physical relationship between the proton backlighter (imploded D^3He-filled capsule), mesh, CH foil, CR-39 imaging detector, and OMEGA laser beams. Distances of the components from the backlighter were 0.8 cm for mesh, 1 cm for foil, and 30 cm for detector. The hole-to-hole spacing in the mesh was 150 μm.

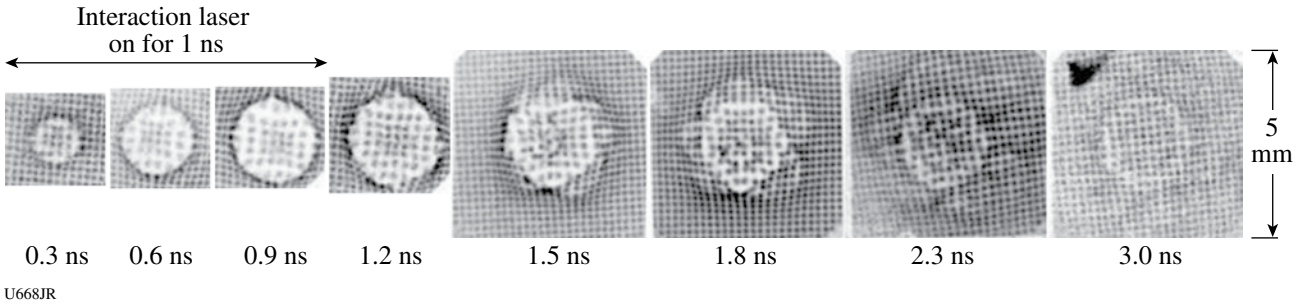

Figure 112.48
Radiographs showing the spatial structure and temporal evolution of the **B** fields generated by laser–plasma interactions. Each image, made with 14.7-MeV protons, is labeled by the time interval between the arrival at the foil of the interaction beam and the arrival of the imaging protons, and each image corresponds to an area about 5 mm by 5 mm at the foil. Note that the laser pulse lasted only 1 ns.

density plasmas. Details and quantitative analysis are given in Ref. 13. In a second series of experiments utilizing 14.7-MeV-proton radiography, multiple laser interaction beams were used simultaneously and resulted in the first direct observation of field reconnection in the high-energy-density regime. Figure 112.49 shows plasma bubbles resulting from two interaction lasers at a time when the bubbles have expanded just enough to contact each other. Quantitative field maps derived from the radiographs revealed precisely and directly, for the first time, the changes in magnetic topology that resulted from reconnection. Details may be found in Ref. 14.

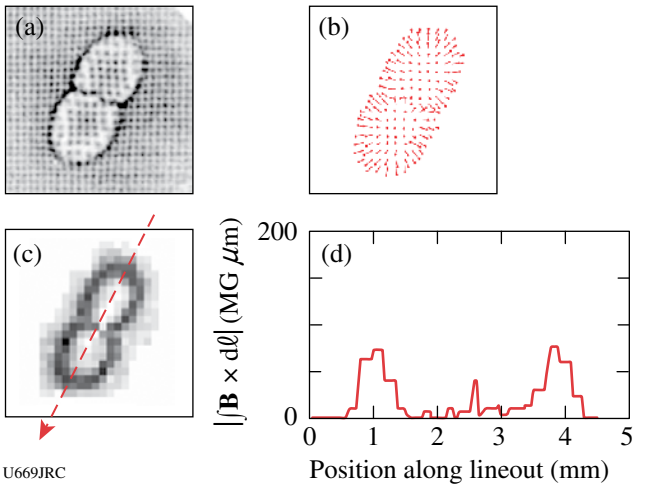

Figure 112.49
A monoenergetic proton radiograph of two plasma bubbles generated in a foil by two interaction lasers was used to deduce a map of the **B** field at the foil. In (a), the location of each beamlet can be compared with the location it would have had with no **B** fields (beamlets on the image edges define the grid of "undeflected" locations); (b) shows displacement vectors. The displacement amplitudes are shown as an image in (c), where each pixel represents one beamlet, with value proportional to displacement. Displacement is proportional to $\int \mathbf{B} \times d\ell$ along the particle trajectory, so the lineout along the arrow in (c) provides quantitative measurements of $\left|\int \mathbf{B} \times d\ell\right|$ at the foil location (d), showing the loss of field energy where the bubbles collided and magnetic reconnection occurred (at about 2.5 mm on the horizontal axis).

X-Ray Compton Scattering on Compressed Matter

Principal Investigators: R. Falcone and H. J. Lee (University of California), P. Neumayer, O. L. Landen, and S. H. Glenzer (LLNL)

These experiments are aimed to measure exact electron density (n_e), temperature (T_e), and ionization (Z) of dense matter with the development of the Compton-scattering technique on the OMEGA Laser Facility. Since an x-ray source can propagate through the critical electron density ~10^{22} cm^{-3}, x-ray Compton scattering has been the most useful diagnostic of local plasma conditions of dense matter with solid density and above. The Compton-scattering cross-section diagnostic is related to the dynamic structure factor $S(k,\omega)$, which presents the Fourier transform of total electron-density fluctuation. It has been understood by decomposing total density distribution: the sum of the motion of electrons and the motion of ions.

Two types of a planar Be target coupled with a Mn backlighter are designed for the x-ray Compton-scattering technique with 90° and 25° scattering angles at the OMEGA Laser Facility. The target consists of a 250-μm-thick Be, 50-μm-thick plastic substrate coated with 3 μm of Mn, 50 μm of Ta with a slot window, and two Au/Fe shields, as shown Fig. 112.50(a). Eleven heater beams of 4-ns flat pulse, $I_{av} \sim 2 \times 10^{14}$ W/cm^2 at 531 nm, are focused symmetrically onto solid Be with an

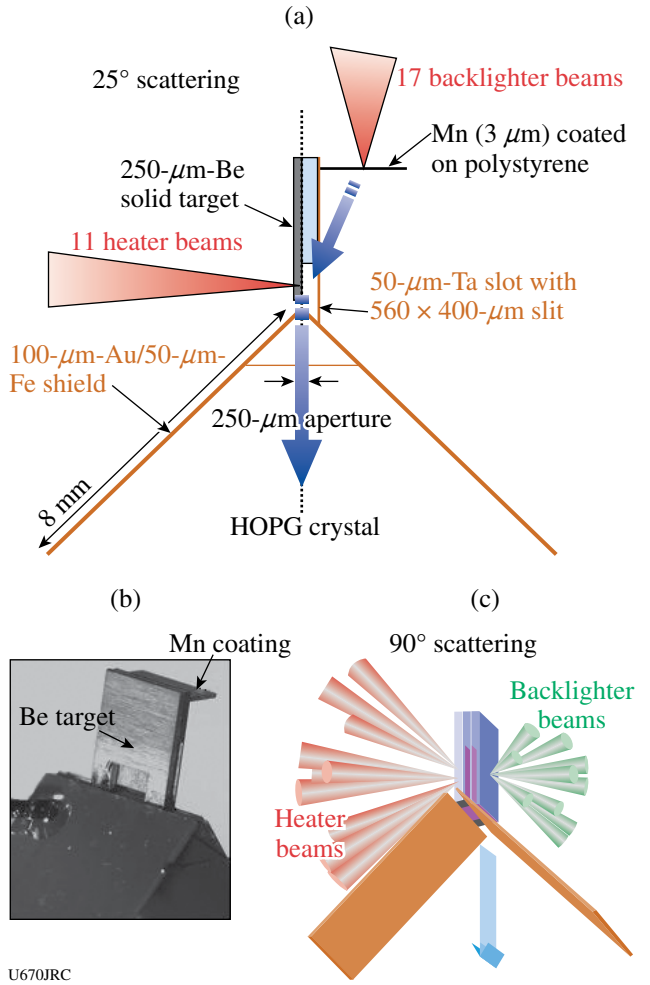

Figure 112.50
(a) Schematic of the target details for 25° scattering; (b) a real image of the target; (c) target schematic for 90° scattering.

~800-μm spot. To create ~6.18-keV Mn He$_\alpha$ x-ray photons, we applied 12 backlighter beams to Mn-coated plastic for 25° scattering (17 backlighter beams for 90° scattering) with a focal spot of 200 μm. Figures 112.50(b) and 112.50(c) present a photograph of 25° scattering target and an image for 90° scattering target that has a Mn backlighter parallel to Be. A highly oriented pyrolytic graphite (HOPG) crystal coupled to an x-ray framing camera with 500-ps gating time in TIM-3 has been used as a spectrometer and a detector.

Figures 112.51(a) and 112.51(b) show scattering spectra (black lines) and fits (thick white lines) to the data of 90° and 25° scattering geometries. In the noncollective scattering regime of 90°, the spectrum shows Compton downshifted peaks in addition to the elastic-scattering peaks at E_{01} = 6.18-keV Mn He$_\alpha$ and E_{02} = 6.15-keV intercombination x-ray lines. With the broadening by the thermal motion of electrons, the intensity and shape of Compton peaks are sensitive to T_e and n_e. For the analysis, we calculated $S(k,\omega)$ theoretical x-ray scattering spectra using the random phase approximation. The calculated spectrum with $n_e = 7.5 \times 10^{23}$ cm^{-3}, T_e = 13 eV, and $Z = 2$ for a Fermi temperature of E_F = 30 eV gives a best fitting to the data. The 25° forward scattering independently provides a unique data set on the n_e and T_e of compressed matter. In the collective scattering regime, the probing wavelength is larger than the Debye screening length and the scattered spectrum is dominated by plasmon resonance, which is associated with electron plasma-wave resonance. The measured spectra of Fig. 112.51(b) show downshifted plasmon peaks; the position of the peak is very sensitive to n_e. The thick white line presents a best fitting to the data. The n_e and T_e measured from the plasmon peak show very good agreement with the parameters obtained from the backscattering spectra as well as from the hydrodynamic calculation on compressed Be plasmas.

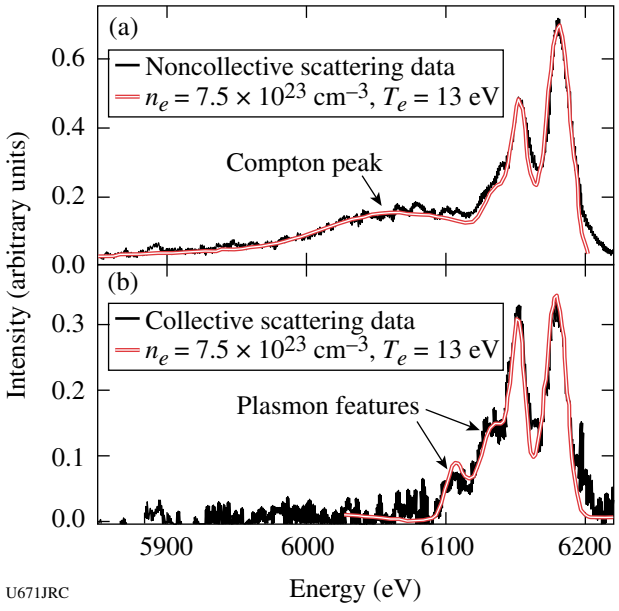

Figure 112.51
Experimental scattering data (black line) and fitting results (thick white line) of (a) 90° scattering geometry and (b) 25° scattering geometry.

Through this project, we successively measured the Compton and plasmon resonance on shock-compressed Be. With the comparison to the theoretical calculation, we find that compressed plasmas of $n_e = 7.5 \times 10^{23}$ cm^{-3}, T_e = 13 eV, and $Z = 2$ within ~15% error bars could be reached under the pressure in the range of 20 to 30 Mbar. From these experiments, we have proved that the x-ray Compton-scattering technique is a precise experimental tool for determining the exact densities and temperatures in compressed matter and characterized compressed states of matter.

FY07 LLNL OMEGA Experimental Programs

In FY07 Lawrence Livermore National Laboratory (LLNL) led 404 target shots on the OMEGA Laser System. This total represents a shot rate approximately 8% higher than nominal (373 shots scheduled for the year). This is an improvement over last year's operations (4% above nominal) and is especially noteworthy considering that programmatic needs frequently require complex configuration changes both overnight and mid-day.

National Ignition Campaign (NIC) Experiments: About 57% of the LLNL shots were dedicated to advancing the National Ignition Campaign in preparation for future experiments at the National Ignition Facility (NIF). This represents a slight percentage decrease from the prior year, as effort transitions to the NIF itself. Campaigns on OMEGA had many objectives, including studies of the laser–plasma interaction (LPI) physics in physical conditions relevant for the NIF ignition targets, improving the diagnostic suite for ignition, and studying dense-plasma physics via collective x-ray scattering; however, this year there was a special emphasis on assessing the physical characteristics of proposed ignition capsule materials.

A variety of LPI experiments were conducted in FY07, some in collaboration with CEA, typically using gas-filled hohlraums arranged so that one OMEGA beam (beam 30) could be used as an on-axis probe beam.

In work now submitted for publication, experiments demonstrated a significant reduction of stimulated Brillouin scattering (SBS) by polarization smoothing in conditions (T_e ~

3 keV) with no ponderomotive and thermal filamentation (see Fig. 112.52). Measurements showed that adding polarization smoothing increases the intensity threshold for SBS by a factor of 1.7. For intensities less than 2×10^{15} W/cm^2, more than an order of magnitude reduction in the backscattered power is observed. This reduction in backscatter was shown to increase the total transmission through a plasma for conditions that are comparable to those in current ICF target designs. A simple model relevant to ICF plasma conditions is able to explain a direct effect on the SBS gain exponent and, consequently, the threshold for when SBS becomes energetically important.

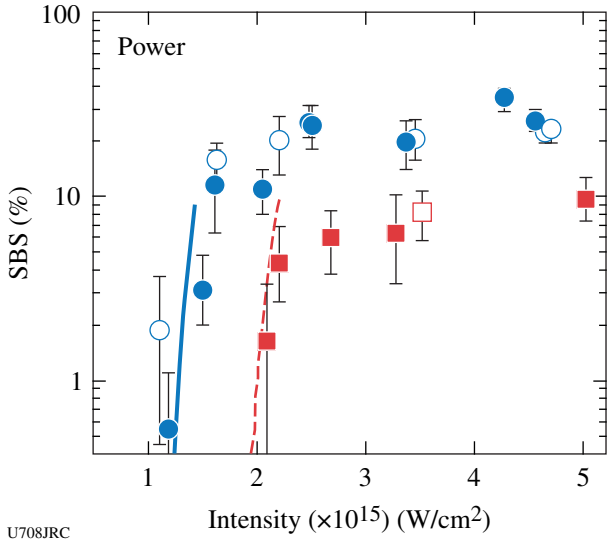

Figure 112.52
The measured instantaneous SBS reflectivity at t = 700 ps is plotted as a function of the interaction beam intensity; three laser-smoothing conditions are shown: continuous phase plates (CPP's, circles), CPP's plus polarization smoothing (squares), and with 3-Å SSD (open symbols). The calculated reflectivities using an analytical model reproduce the measured thresholds and a factor-of-1.7 reduction in the SBS threshold when polarization smoothing is applied to a CPP-smoothed laser beam. An analytical model that calculates the thresholds is shown for the CPP only (solid curve) and when polarization smoothing is applied (dashed curve).

Another experimental result now submitted for publication, and detailed in Fig. 112.53, extends the limits of plasma length in inertial fusion laser–plasma interaction experiments. Laser-beam propagation and low backscatter were demonstrated in laser-produced hohlraum plasmas of ignition plasma length. At intensities $<5 \times 10^{14}$ W/cm^2, greater than 80% of the energy in a blue (351-nm) laser is transmitted through an L = 5-mm-long, high-temperature (T_e = 2.5 keV), high-density ($n_e = 5 \times 10^{20}$ cm^{-3}) plasma. For an intensity of $I = 6 \times 10^{14}$ W/cm^2, these experiments also show that the backscatter scales exponentially with plasma length, from <0.05% at a 1.3-mm length to >10%

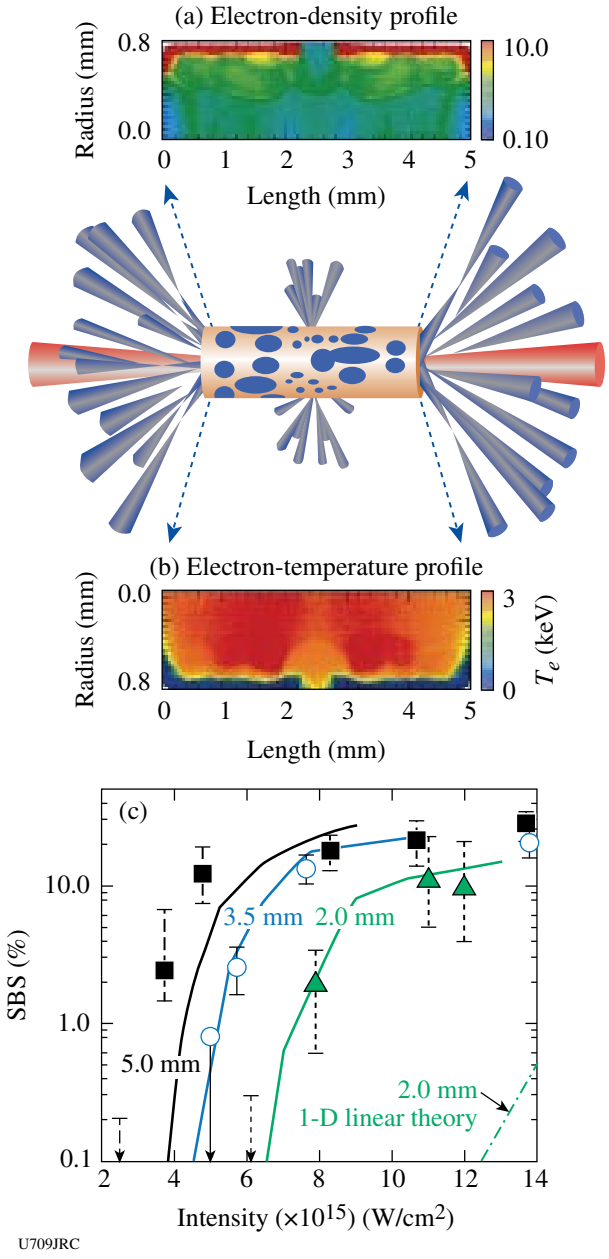

Figure 112.53
(a) Simulated electron-density and electron-temperature profiles for a 5-mm-long LPI hohlraum at peak electron temperature (900 ps after the heater beams turn on). Three LEH's are equally spaced around the hohlraum equator to allow the addition of 17 laser beams. In total, 53 laser beams irradiate the hohlraum wall, producing electron temperature T_e along the axis in excess of 2.5 keV. The interaction beam is aligned along the axis of the hohlraum, interacting with a uniform 5×10^{20} cm^{-3} plasma plateau. (b) The measured instantaneous SBS reflectivity is plotted as a function of vacuum intensity for the three target lengths: 2 mm (triangles), 3.5 mm (circles), and 5 mm (squares). The solid curves are simulations performed by SLIP. For reference, a line is shown (dashed–dotted) calculated using linear theory for the 2-mm-long targets where a gain of $\Gamma_s \beta_s = 11$, for an intensity of 1×10^{15} W/cm^2, is determined by post processing the hydrodynamic parameters.

at a 4.0-mm length. This result is consistent with linear theory. The backscatter calculated by a new steady-state, 3-D laser–plasma interaction code (SLIP) developed for large ignition plasmas is in good agreement with the measurements. These results span the gap between previous studies ($L < 2$ mm, $T_e = 2.5$ keV) and future ignition hohlraum plasmas ($L = 5$ mm, $T_e > 3$ keV) and indicate that backscatter can be controlled at ignition plasma conditions and intensities.

Additional laser–plasma interaction experiments on the high-electron-temperature gas-filled hohlraum target platform demonstrated the effectiveness of Landau damping in multiple-ion species plasmas to reduce backscatter. By adding hydrogen to a CO_2 gas fill, the SBS reflected power was suppressed from >30% to ~1%, while SRS was below the detection threshold (Fig. 112.54). Improved heater beam coupling into the hohlraum by suppression of the total backscatter resulted in an increase in measured hohlraum radiation temperature. As a result of these findings, a multiple-ion-species gas fill is now included in the NIC hohlraum point design.

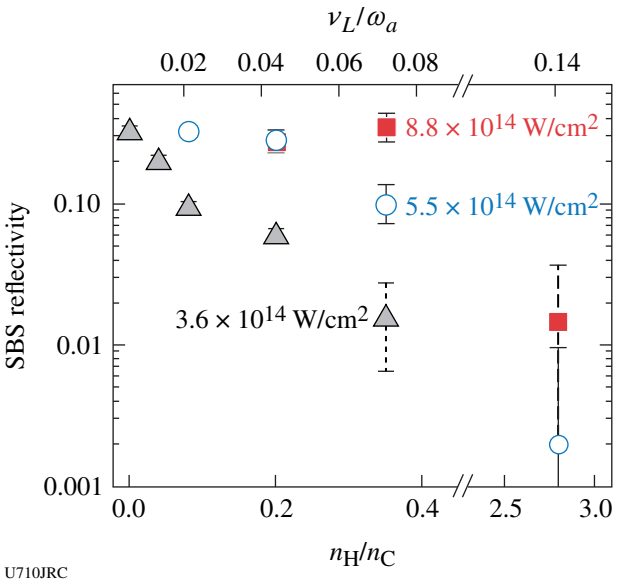

Figure 112.54
The SBS reflectivity is reduced from >30% to ~1% when increasing Landau damping by adding hydrogen to the CO_2 hohlraum gas fill (probe-beam intensities of 3.6, 5.5, and 8.8×10^{14} W/cm^2).

In pursuit of a more precise understanding of hohlraum energetics, and to develop methods for diagnosing possible ignition failure modes, half of an extended day was dedicated to a series of shots designed to study the impact of x-ray flux originating from outside the laser entrance hole (LEH) of a laser-heated hohlraum—measured with the OMEGA Dante diagnostic—on the interpretation of the observed radiation temperature inside the hohlraum. An empty gold hohlraum was heated with 38 beams using a 2.6-ns-long pulse. In addition, two beams were used to illuminate the hohlraum outside of the LEH. One beam had a large spot size, mimicking the effect of LEH closure during the heating; the second beam had a small spot size, providing an indicator of the x-ray emission due to a mispointed heater beam. A soft x-ray imager was used to identify the various sources of x-ray emission, and Fig. 112.55 shows a set of images for three different x-ray regimes, i.e., around 250 eV, 750 eV, and above 2 keV. For this particular shot, the start times of the cone 2 and cone 3 heater beams were tuned to also study the spot formation. The series of shots indicated that without correcting the x-ray flux measured by Dante with respect to its origin, the derived radiation temperature was about 1% higher.

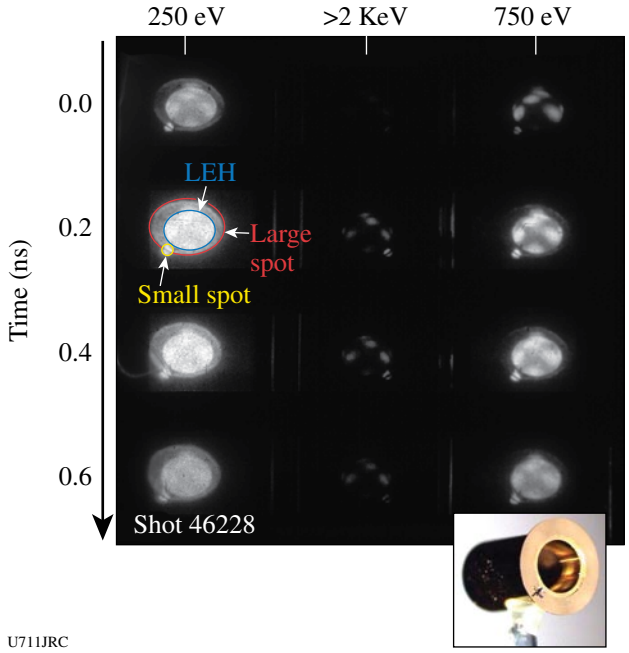

Figure 112.55
Soft x-ray images taken from the laser-heated Au hohlraum, together with a picture of the target. The x-ray images show the emission from the LEH with various spots from the heater beams. Additional x-ray emission originates from a large beam spot and a small beam spot, which hit the gold washer and provide the required emission area outside of the LEH to mimic the "LEH closure" scenario. The washer also contains a spatial fiducial (cross hair).

Progress also continued in characterizing the physical properties of warm, dense matter. Experiments studying x-ray scattering on radiatively heated solid-density beryllium at different scattering angles provided a first direct test of dense matter theories describing ion–ion correlations at long scale lengths in dense matter, as shown in Fig. 112.56.

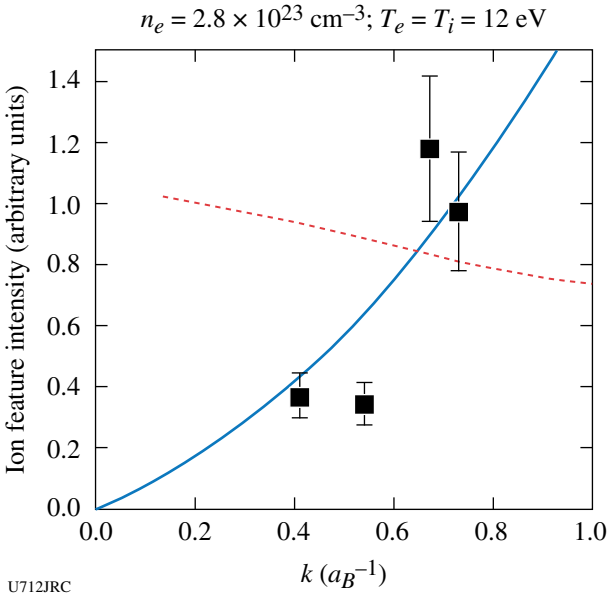

Figure 112.56
Comparison of measured elastic scattering feature with theoretical predictions, showing better agreement with the HNC TCP calculations.

Ignition capsules face challenging physics requirements since they must transmit shocks into the DT ignition fuel without also producing hydrodynamic instabilities that would dilute the fuel with higher-Z ablator material. This translates into requirements for very low surface roughness and specific shock response properties. In FY07, the physical properties of capsules based on copper-doped beryllium and high-density carbon (synthetic diamond) were studied extensively, using new techniques that significantly extend previous work on, e.g., Rayleigh–Taylor growth measurements, imploding-capsule radiography, and velocity interferometry of shocked surfaces.

Simulations predict that residual microstructure and velocity fields in melted Be could still seed some hydrodynamic instabilities upon shock breakout, but at a level below that expected and acceptable from growth of known surface imperfections. To validate these expectations, we have designed OMEGA experiments that amplify their perturbation seeding using high-growth-factor [GF ~ exp($\gamma\tau$)] Rayleigh–Taylor instability drives. To achieve this, an 8- to 10-ns-long drive has been developed [see Fig. 112.57(b)], which for a given achievable radiographic accuracy, ΔGF/GF = $\tau\Delta\gamma$, leads to an improved growth-rate accuracy $\Delta\gamma \sim 1/\tau$. This drive also provides sufficient sensitivity to directly measure, through x-ray radiography, 3-D growth from BeCu planar foils with a level of surface roughness equal to the NIF ignition design surface-roughness tolerance [see Fig. 112.57(c)]. The results—when compared to simulations that ignore possible growth from

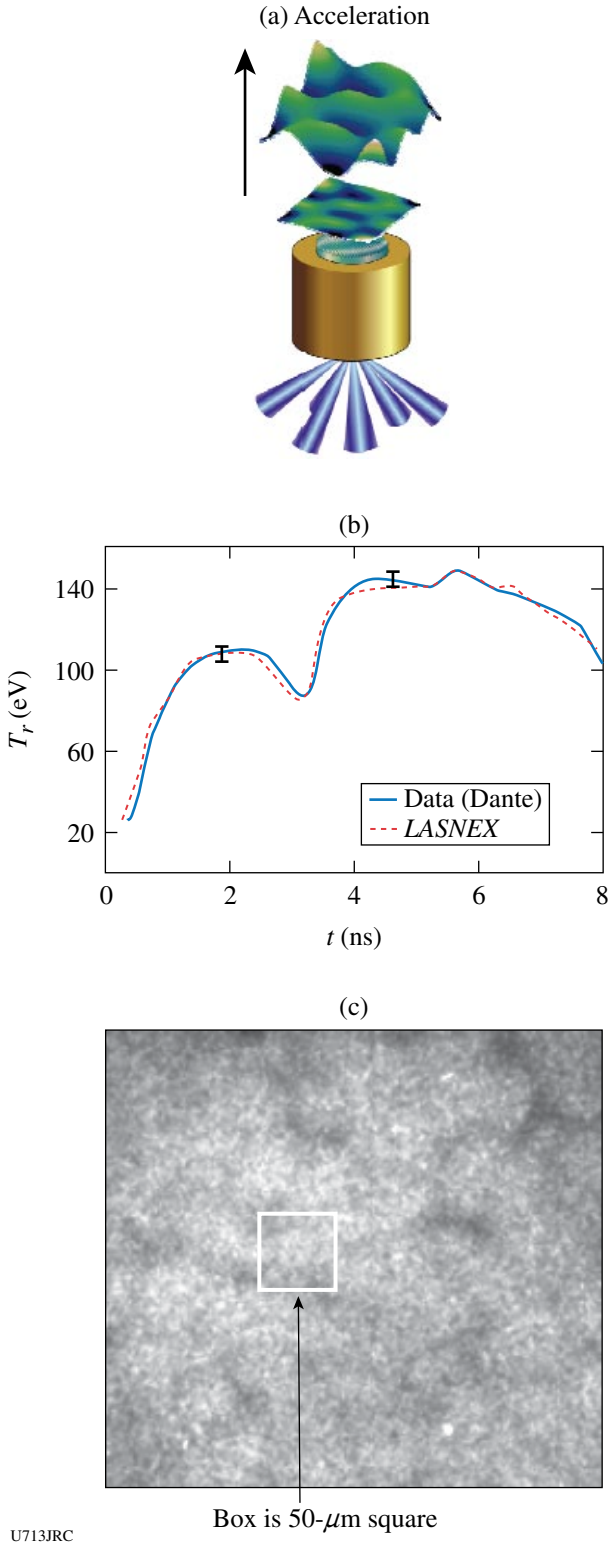

Figure 112.57
(a) Experimental setup for ablation-front Rayleigh–Taylor growth measurement; (b) measured versus calculated x-ray drive T_r; (c) 4.3-keV radiograph of growth of NIF-surface roughness on Be(Cu) foil at 8.2 ns.

Be microstructure and, therefore, consider only growth from surface perturbations—suggest that, at least for ablation-front instability growth, microstructure is not important.

Determining ablator performance during an implosion is a critical part of the NIF tuning campaign. In particular, it is vital to have accurate, time-resoved, in-flight measurements of the velocity, areal density, and mass of the ablator as it converges. In tests on OMEGA we have developed a new technique that achieves time-resolved measurements of all these parameters in a single, area-backlit, streaked radiograph of an indirectly driven capsule. This is accomplished by first extracting the radial density profile at each time step from the measured radiograph; then scalar quantities such as the average position, thickness, areal density, and mass of the ablator are determined by taking integral moments of this density profile. Results from implosions of Cu-doped Be capsules are shown in Fig. 112.58.

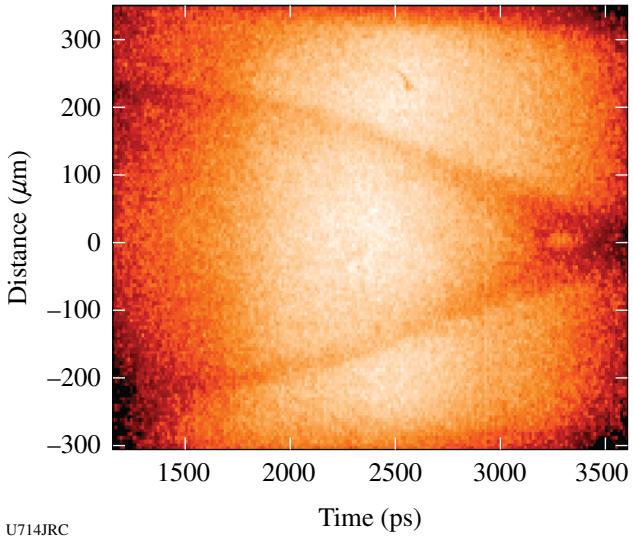

Figure 112.58
Streaked radiograph showing converging capsule leading up to bang time at 3300 ps.

Synthetic diamond is a promising ablator material for ICF capsules because of its low-Z and high density. It is important, however, to know the high-pressure phase diagram of diamond since the tuning design for ICF capsules requires that the first-shock state remain completely solid and the second-shock state be completely melted. Having successfully measured first-shock melting of diamond on OMEGA last year, a new method was developed this year to detect second-shock melting. This involved launching a first shock into diamond between 2 to 4 Mbar, followed by a strong second shock between 15 and 25 Mbar. As shown in Fig. 112.59, by measuring the thermal emission of the second shock through the transparent first shock, it was possible to determine the temperature of the second-shock Hugoniot versus pressure. Evidence of melting was found in the discontinuity in the second-shock Hugoniot above 20 Mbar.

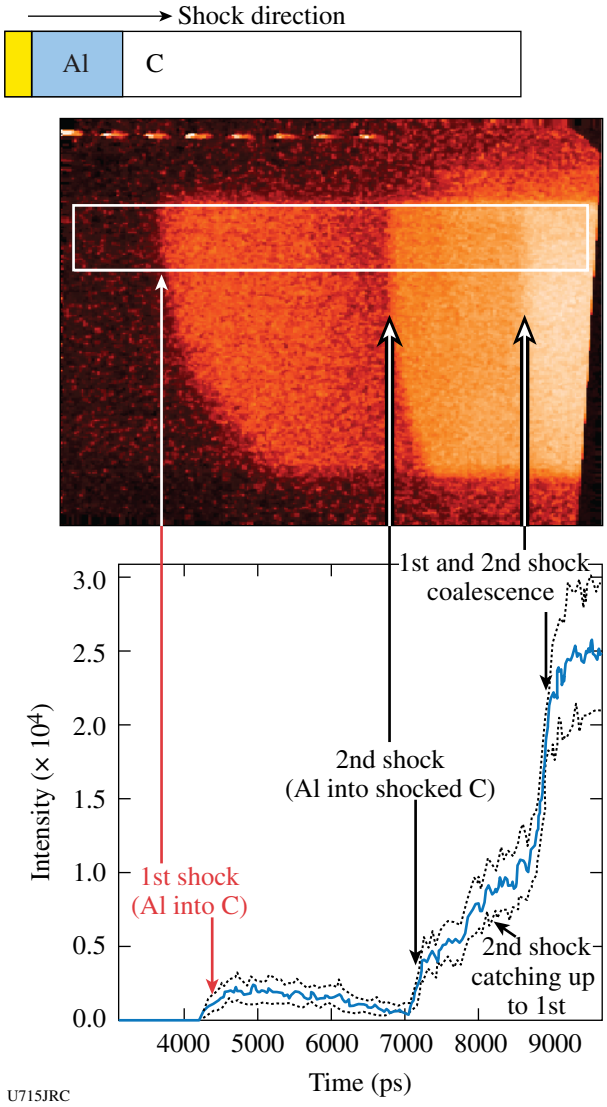

Figure 112.59
Streaked, space-resolved measurement of the thermal emission from a doubly shocked Al/diamond sample.

Determining the level of velocity uniformities created by microscopic perturbations in NIF ablator materials is a challenging measurement task. The measurement diagnostic must detect these nonuniformities at a level of a few parts in 10,000 to be relevant to the NIF requirements. The CAPSEED campaigns were fielded to make these measurements with a

new technique. During FY07 a high-resolution velocity interferometer was fielded on the TIM-6 diagnostic location. The instrument, called the OMEGA High-Resolution Velocimeter (OHRV), is a 2-D space-resolving "velocity interferometer from the surface of any reflector" (VISAR), which probes the velocity distribution across a moving reflecting surface with 2-μm spatial resolution and few-m/s velocity resolution in a single 2-D snapshot. Its main mission is to measure the seed-level nonuniformities in NIF capsule ablator candidate materials and to verify that the seed levels are consistent with current model predictions of capsule performance. Assembly and qualification of the instrument took place during the summer, commissioning in early September, followed by a successful experimental campaign in October (Fig. 112.60). Experiments testing Be(Cu), high-density carbon, and Ge-doped plastic ablators are continuing in FY08.

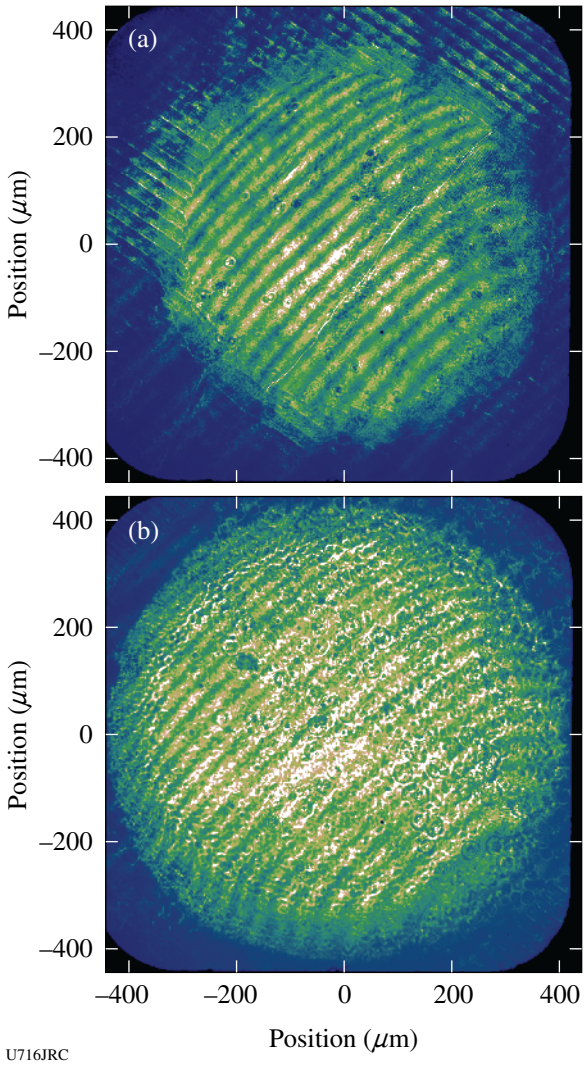

High-Energy-Density Science (HEDS) Experiments: About 43% of the LLNL shots were dedicated to HEDS campaigns, including quasi-isentropic compression experiments (ICE), dynamic hohlraums, opacity measurements of hot plasmas in local thermodynamic equilibrium (LTE), and non-LTE implosion physics. High-temperature hohlraums, long-duration point backlighter sources, and foam-walled hohlraums were also studied to develop HED experimental platforms for future NIF experiments.

LLNL has for some time been developing laser-based experimental platforms that can compress materials quasi-isentropically to very high pressures at ultrahigh strain rates. This laser-driven, ramped (shockless) drive is used to study material properties such as strength, equation of state, phase, and phase-transition kinetics under extreme conditions. In FY07 an effort was launched to develop a platform compatible with NIF, based on ICE drive by indirect x-ray illumination from a hohlraum onto a reservoir/package assembly on the side of the hohlraum at the midplane.

Development of such a hohlraum-driven ICE platform requires an understanding of the hydrodynamics of hohlraum radiation coupling to the ICE pressure, planarity of the pressure drive on the package, hohlraum filling at late times for package radiography, and potential preheat of the reservoir and package by the hohlraum M band.

Initial experiments used the normal OMEGA VISAR (ASBO) system and a tilted target package (since the VISAR does not have a view orthogonal to a standard hohlraum axis). This approach provided helpful information on obtaining VISAR data from hohlraum packages, but it resulted in hard-to-model 3-D effects on the drive and insufficient planarity. A new tilted ASBO telescope was developed that is able to measure packages normal to the hohlraum axis. It has now been tested and fully qualified for the next set of experiments, presently scheduled for January 2008.

Figure 112.60
(a) Two-dimensional interferogram of a shock front emerging from a Be(Cu) ablator sample approximately 200 ps after breakout into a plastic layer (central 600-μm-diam circular region). Bias fringes run from bottom left to top right; a preimposed ripple machined into the Be surface is visible in the edges of the image (periodic pattern oriented perpendicular to the fringes). (b) Velocity interferogram of a shock front emerging from a diamond ablator into a plastic layer, approximately 1 ns after breakout. The high-frequency spatial modulations superimposed on the fringe pattern indicate nonuniformities in the shock front.

A parallel set of experiments studied the hohlraum plasma filling at late times. Hohlraums with and without thin CH liners were probed using a 6.7-keV Fe backlighter. The radiographic data were used to assess the Au filling from the walls at late times (t = 20, 60, and 80 ns after the hohlraum drive); these results agreed well with 2-D simulations. The hohlraum stays open at late times with minimal filling, providing support for future ICE-driven Rayleigh–Taylor radiography experiments at late times on the NIF.

To understand the drive on the reservoir, the radiation temperatures of different types of hohlraums were studied and compared with *LASNEX* 2-D simulations. Figure 112.61 shows the Dante measurements and *LASNEX* simulations from both CH-lined and non-CH-lined hohlraums. The peak radiation temperature data are in good agreement with the simulation, but the simulation shows the radiation temperature remaining higher later in time than the data indicate. This might be caused by the on-axis stagnation effect, which is more pronounced in the symmetric 2-D simulation as opposed to the experiments, which have enough 3-D effects to reduce the axial stagnation. The study of late-time hohlraum energetics is significant for multiple HEDS campaigns and will continue in FY08.

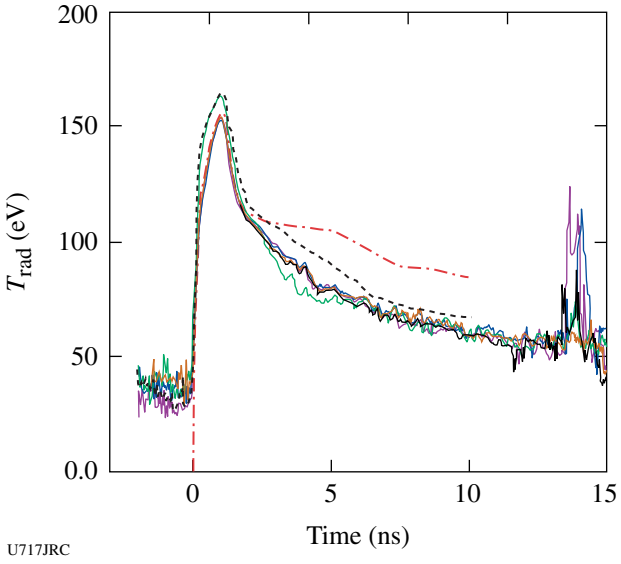

Figure 112.61
Dante radiation-temperature measurements (solid) from scale-1.37 hohlraums driven with 12.5 kJ in a 1-ns square pulse, compared with 2-D *LASNEX* simulations (dashed).

Over the past year, LLNL has continued experiments with laser-driven dynamic hohlraums (LDDH's). These experiments have compared the neutron yield and the areal fuel density produced by "standard" xenon-filled LDDH's (see Fig. 112.62) to those of capsules where the xenon is replaced by neopentane; the latter gas fill replicates the hydrodynamics of a xenon-filled LDDH but does not create the high-Z radiation-trapping cavity (hohlraum), thus making it possible to measure the difference in yield and fuel density due to the hohlraum effect. Analysis of this data is underway. Additional LDDH experiments have explored the robustness of dynamic hohlraums when driven by laser beams in a polar configuration, such as would be necessary on the NIF; the experiment showed that repointing the laser beams along the polar axis can compensate for the nonuniform laser drive.

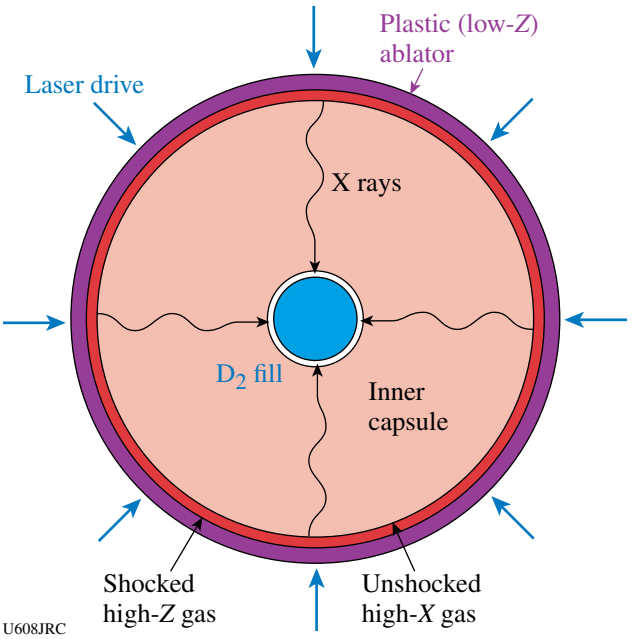

Figure 112.62
Concept of "dynamic hohlraum:" shock-heated Xe gas between shells radiates x rays that ablatively implode inner shell. Data obtained include x-ray-streaked images of the self-emitted x rays, multiple x-ray images, charged-particle information (collaboration with MIT), and multiple standard OMEGA neutron diagnostics.

Prior results having shown that LDDH's emit very bright, spectrally smooth bursts of multi-keV x rays, it was decided to explore whether LDDH's might scale down for use as bright, broadband backlighters suitable for absorption spectroscopy experiments. Early in FY07, a set of small, Kr-filled plastic capsules were imploded using ten polar direct-drive beams and produced bright continuum emission at photon energies up to at least 5.5 keV (Fig. 112.63). These capsules proved bright enough to be used as backlighters for spectroscopic transmission measurements of hot plasmas. Previous continuum x-ray sources either required too many beams (so that the hot plasmas

could not be produced) or did not work at photon energies above ~3500 eV (Ref. 18). In a follow-up experiment, initial data were obtained for $n = 1$ to $n = 2$ absorption of Ti samples at LTE conditions near 100 eV inside hohlraums. LLNL plans to use this new capability to measure the temperatures of high-temperature LTE opacity samples in FY08.

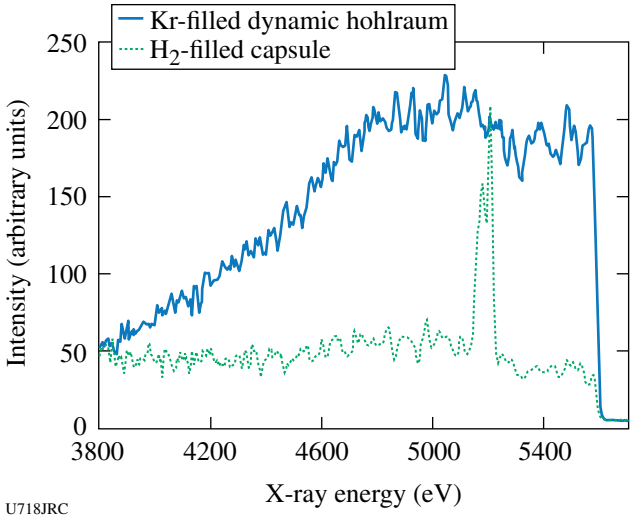

Figure 112.63
Gated spectra produced by an H_2-filled capsule (dotted) and a Kr-filled capsule (solid). Instrument configurations were identical for both shots; Dante data for this band show a factor-of-2 increase in peak x-ray yield. The lines near 5200 eV in the H_2 spectrum are from a vanadium dopant in the shell for that capsule.

The goal of the nonlocal thermodynamic equilibrium (NLTE) campaign is to build a platform to study energy balance in implosions by measuring ion, electron, and radiation temperatures as a function of high-Z dopant concentration. In the FY07 experiments, all 60 beams of the OMEGA Laser Facility were used for direct-drive implosions of thin (4 μm) glass capsules filled with 10 atm of D^3He gas and 0.01 atm of Kr gas as a spectroscopic tracer. We used Xe as the high-Z dopant gas, with concentrations from 0 to 0.06 atm. As a time-resolved electron-temperature (T_e) diagnostic, we fielded a new mica conical crystal spectrometer (Fig. 112.64), which was coupled to a streak camera, and viewed K-shell emission lines from the Kr dopant. Time-integrated spectra were also recorded with the HENEX spectrometer developed by NIST/NRL. The time-resolved spectra show that the addition of Xe reduces T_e proportionally, in agreement with simulations. Time-dependent ion temperatures (T_i), inferred from proton and neutron emission time histories and spectra, also show a reduction in the compression-phase T_i with increasing Xe concentrations. Finally, secondary neutron measurements as well as gated x-ray

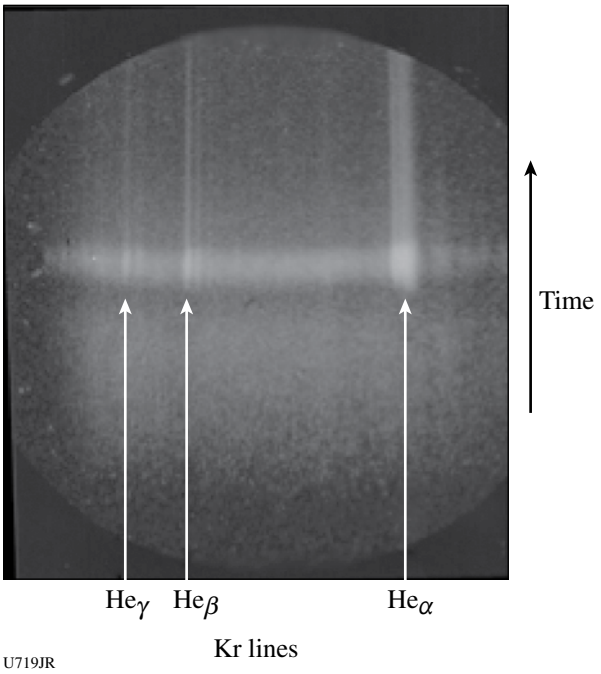

Figure 112.64
Typical time-resolved spectrum from the mica conical crystal spectrometer for a capsule without Xe dopant.

pinhole images show a dramatic reduction in areal density and core size as the Xe concentration is increased.

One of the campaigns planned for the NIF will study the opacities of high-temperature plasmas in LTE conditions. Present-generation long-pulse facilities produce LTE plasmas in the range of 100 to 180 eV, and the intent is to extend this range upward on the NIF. To do so, it is desirable to optimize the coupling of high-intensity laser radiation to produce x rays from small targets, which in turn heat samples in LTE conditions. In FY07 the high-temperature hohlraum development campaign began studying the utility of rear-wall burnthrough radiation from the back of a small halfraum as a technique for radiatively heating samples several hundred microns away. Figure 112.65 shows data from plastic (carbon) and chromium samples diagnosed with x-ray spectroscopy. Surprisingly, the samples were cooler (under-ionized) relative to what was predicted. Future work will focus on improving the modeling to match the observations and then looking for ways to optimize the experimental configuration.

To produce multiple radiographic images with a single NIF shot, with a minimum number of NIF beams devoted to the backlighter, it is desirable to have a long-duration point-projection backlighter source. To this end, a few half-days were devoted to developing a long-duration, pinhole-apertured,

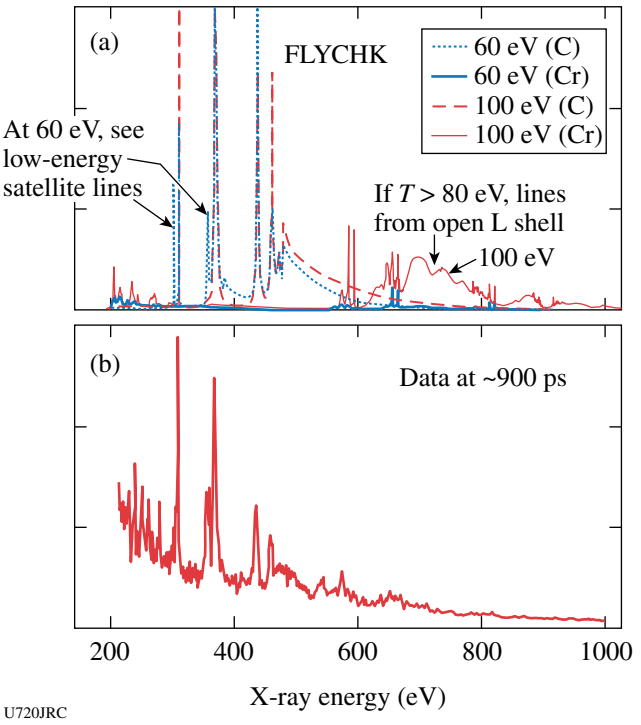

Figure 112.65
(a) Spectroscopic data from a target radiatively heated by the thin back wall of a tiny holraum. (b) Comparison with modeling indicates target temperature is 60 to 70 eV at this time.

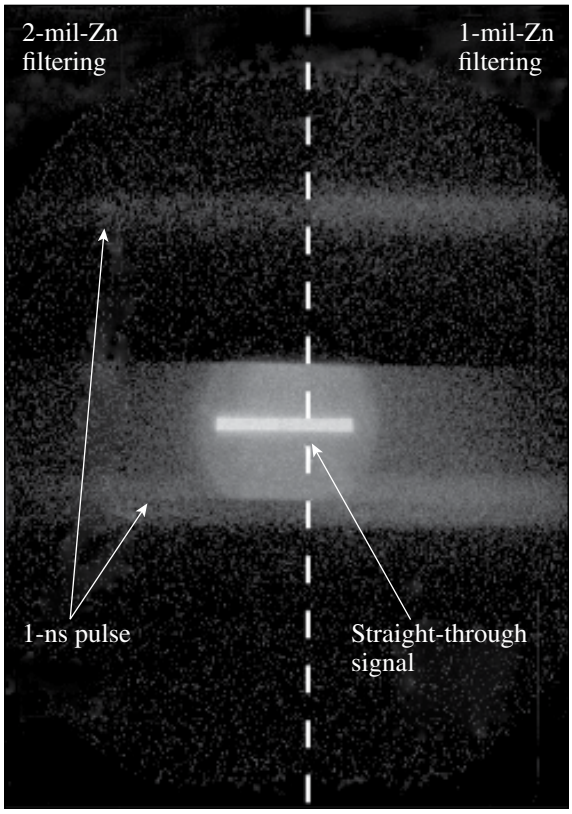

Figure 112.66
Streak measurement of Zn backlighter radiation from multiple OMEGA laser pulses, demonstrating adequate signal-to-test, long-duration backlighter concepts for the NIF.

point-projection zinc K-shell backlighter to diagnose NIF experiments. Current laser experiments use pulses of typically 0.2 to 1.0 ns. Extending the backlighter duration out to the desired 8 ns for the NIF leads to issues of pinhole closure and signal strength. Initial experiments using a streak camera with an open slit showed a significant contribution to the background from the streak camera's retrace signal. Subsequent experiments (Fig. 112.66) showed that increasing the laser intensity on the backlighter and using zinc filtering to block unwanted low-energy radiation was sufficient to produce an adequate signal above the retrace and other backgrounds. The continuation of this campaign in FY08 will explore pinhole closure time and new backlighter designs aimed at increasing the signal-to-noise ratio without sacrificing resolution.

To further improve hohlraum heating efficiency and reduce plasma filling (which obscures radiographic views of HED material samples), hohlraum development experiments have been conducted using laser-driven cylindrical hohlraums whose walls were machined from Ta_2O_5 foams of 100-mg/cc and 4-g/cc densities. Measurements of the radiation temperature, shown in Fig. 112.67, demonstrate that the lower-density walls produce higher radiation temperatures than the higher-density

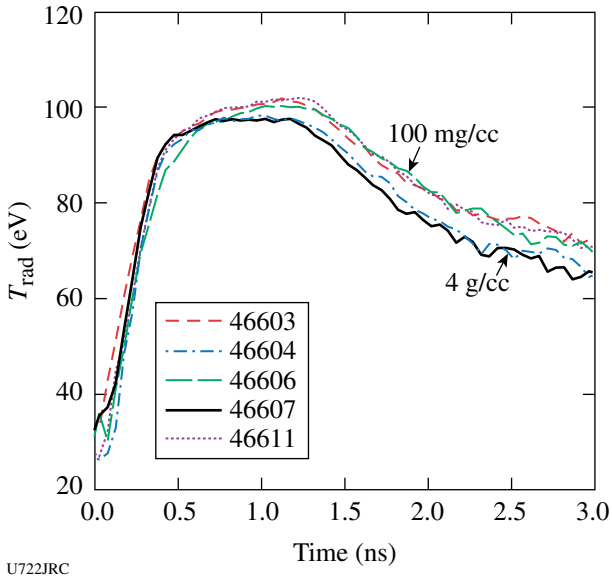

Figure 112.67
Radiation temperature from Dante measurements for five foam-walled hohlraums.

walls. The difference in temperature is determined by the difference in energy lost to the walls. For higher-density walls, the radiation front propagates subsonically, so the density seen by the front is dominated by the density profile established by the rarefaction wave. For lower densities the radiation-front velocity is supersonic so the energetics of the wall are determined by the equation of state and the opacity of the wall material.

FY07 LANL OMEGA Experimental Programs

During FY07 Los Alamos National Laboratory (LANL) successfully fielded a range of experiments on OMEGA to study the physics relevant to inertial confinement fusion (ICF) and high-energy-density laboratory plasmas (HEDLP) in support of the national program. LANL conducted a total of 192 target shots on OMEGA, 22% higher than the nominal allocation. Collaborations with LLNL, LLE, MIT, and AWE remain an important component of LANL's program on OMEGA. In particular, the LANL-led symergy campaign has provided a better understanding of symmetry control for the future NIF ignition experiments.

Radiation Transport in Inhomogenous Media: The inhomogeneous radiation flow experiment was allotted a single shot day in FY07. This experiment studies the transport of radiation through inhomogeneously mixed media; that is, where discrete particles of random size are randomly dispersed in a host material. For a constant gold fraction, the effective opacity of the mixture is expected to increase as the particle size decreases, thereby slowing the radiation propagation in the media. Many models describe this phenomenon,[19–24] but it has not been demonstrated that these models are implemented correctly in our codes.

The radiation source for these experiments is a hohlraum nominally heated by 7.5 kJ of laser energy to a peak temperature of about 210 eV (Fig. 112.68). The radiation from the hohlraum drives a temperature front into a gold-loaded foam. The foams are nominally 55 to 60 mg/cm^3 of triacrylate ($C_{15}H_{20}O_6$) foam containing nominally 12% by atom gold particles. The size of the gold particles is varied during these experiments to observe how the particle size impacts the temperature-front propagation.

An example of the effect the gold particle size has on the temperature-front propagation is shown in Fig. 112.69. The data clearly show this effect for the temperature-front propagation for two gold particle cases: 5-μm diameter and atomic mix. At early times, the temperature-front propagation is similar; however, at 2.5 ns there is roughly a 100-μm difference between the two cases. Also, simulations with the Langrangian radiation hydrodynamics code NYM[25] (Fig. 112.70) show excellent agreement with the experimental data in the atomic-mix case.

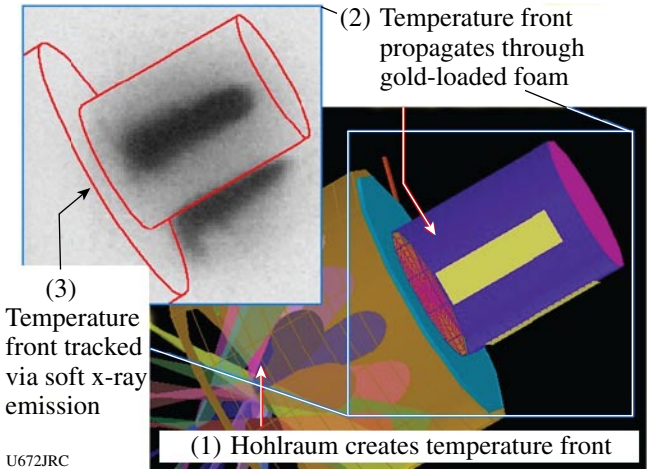

Figure 112.68
A schematic of the inhomogeneous radiation flow platform.

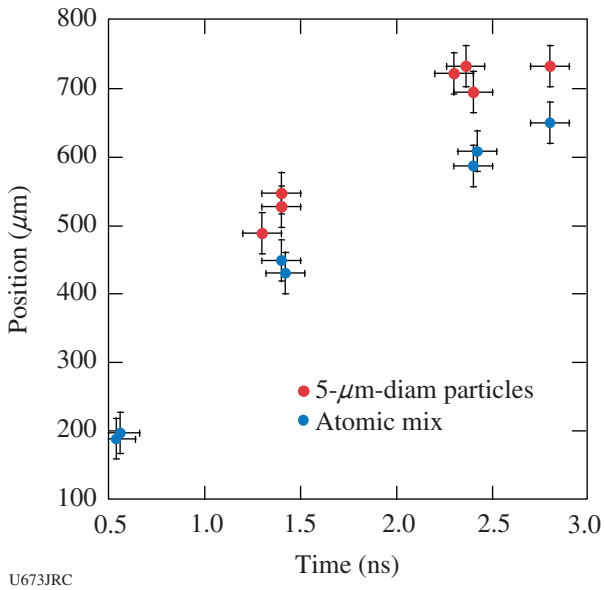

Figure 112.69
Experimentally determined temperature-front position showing the differences between foams loaded with 5-μm-diam gold particles and an atomic mix with gold particles. By 2.5 ns, the temperature front has propagated 100 μm farther in the 5-μm particle case than in the atomic-mix case.

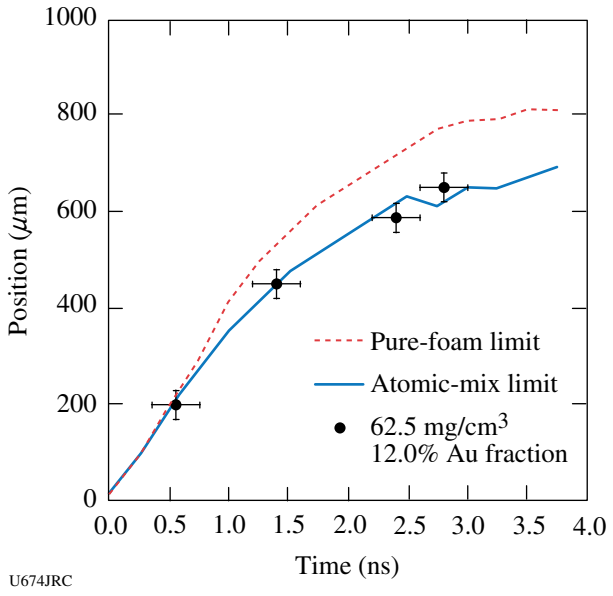

Figure 112.70
A comparison of the simulation in the pure-foam and the atomic-mix limits versus the experimental data. The atomic-mix simulation is in excellent agreement with the experimental results.

Off-Hugoniot Experiments: Recent experiments by LANL on OMEGA explored the hydrodynamic evolution of embedded layers subject to radiative heating. These experiments, focusing on hydrodynamic evolution, are being used for quantitative validation of 3-D Advanced Scientific Computing (ASC) calculations of both large- and small-scale hydrodynamic motion. In contrast to traditional shock-interaction experiments, the material conditions are constantly changing with time before and during the shock-interaction process. The complex material and density gradients developed during the heating phase significantly change the shock evolution from what it would be with the initial "as-built" profile. Thus far, the types of embedded features fielded include planar disks, rectangular gaps, and, most recently, single-mode sinusoids. This campaign began in 2004 and continues today with significant collaboration from the Atomic Weapons Establishment (AWE). Current efforts have shifted from data collection to analysis and quantitative comparison with simulations. In FY07 LANL conducted two days of shots on OMEGA that yielded high-quality images of both heated and shocked-gap targets as well as newly fielded sinusoid targets (Figs. 112.71 and 112.72). Data from the sinusoid targets show a recurring phase inversion of the sinusoid pattern as predicted by 3-D ACS calculations.

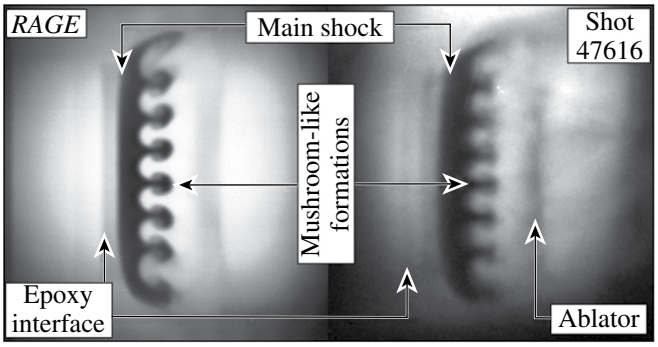

Figure 112.72
Comparison of 3-D ASC *RAGE* calculation (left) with experimental data (right) of heated and shocked sinusoid targets.

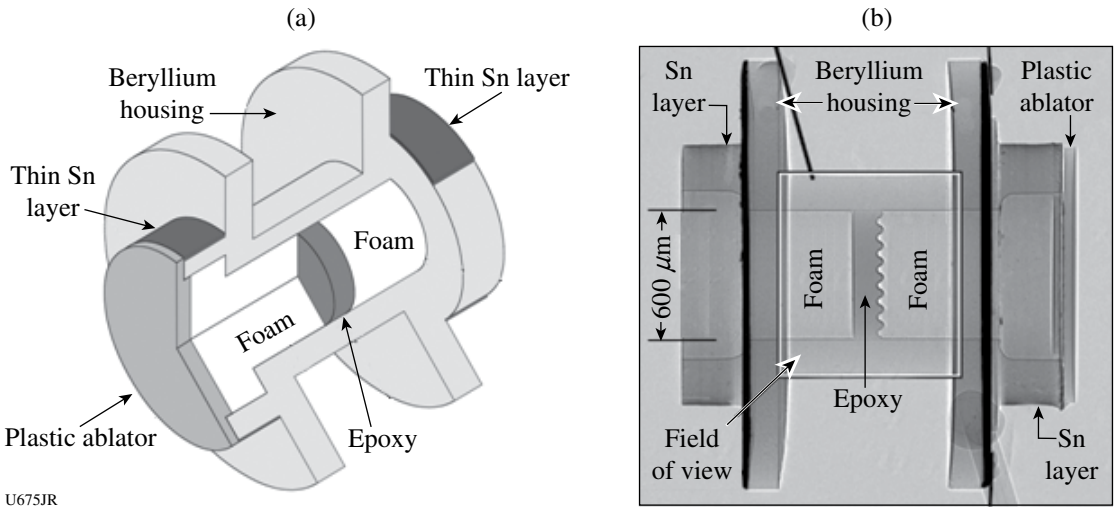

Figure 112.71
(a) Targets consist of a Be housing with epoxy between 60-mg/cm^3 foam parts. A plastic ablator is used to generate shocks. (b) Full target characterization is performed before shots including radiographic images to determine part alignment and material impurities.

NIF Platform #5: The NIF Platform #5 (NIF 5) Campaign is developing x-ray diagnostic techniques to measure temperature in radiation-transport experiments on the future National Ignition Facility (NIF). In FY07 NIF 5 had 1.5 shot days and obtained extremely useful data. This year NIF 5 met both of its main objectives: to measure the spectrum of a suitable backlighter source and to determine the temperature of a foam that had been radiatively driven.

The NIF 5 platform (Fig. 112.73) utilizes a quasi-continuum backlighter and a hohlraum to heat a low-density foam. In some configurations, the backlighter alone is used to measure its x-ray emission spectrum.

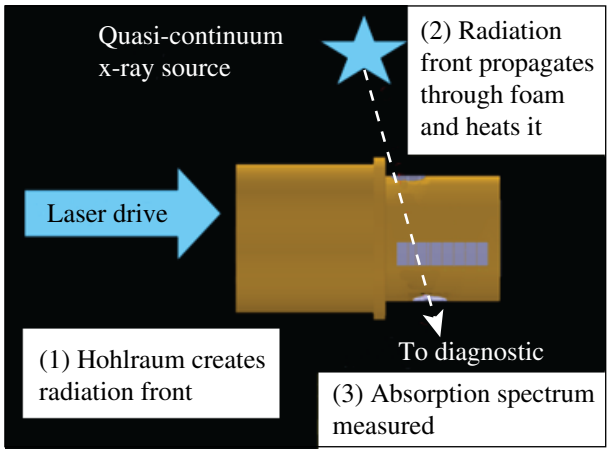

Figure 112.73
A schematic of the NIF 5 platform experimental configuration.

Figure 112.74 displays an example of the absorption data obtained. The emission present is due to the M-band emission of the gold backlighter. The backlighter emission was initiated before the foam was heated and continued during the heating

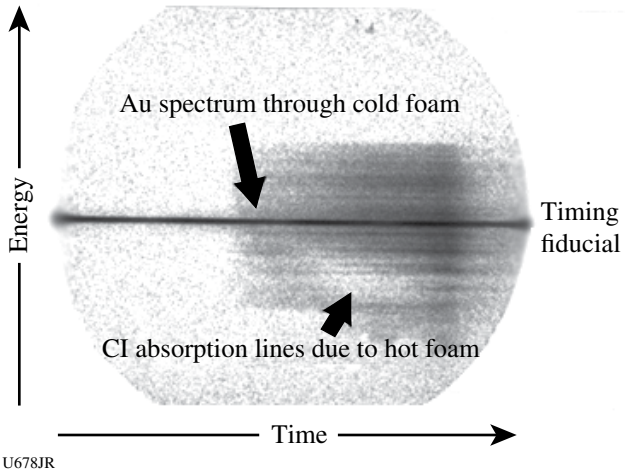

Figure 112.74
Measured absorption spectrum due to a heated foam. The vertical axis is the spectral energy (increasing to the top) and the horizontal axis is time (increasing to the right). The emission is due to the M band of the gold backlighter.

phase of the foam. As the foam heats, the absorption spectrum profile changes, which is captured by the data.

Symergy: LANL fielded two days of OMEGA experiments to test the concept of using thin shells to quantify asymmetry during the foot of the NIF pulse in support of the National Ignition Campaign. Figure 112.75 shows the ~0.7-scale NIF hohlraum geometry used for these experiments. Three cones of beams enter the hohlraum from each side with a 3-ns laser pulse to produce a peak radiation temperature of ~115 eV, comparable to the foot pulse incident on an ignition capsule.

The emission levels from the capsule implosions (Fig. 112.76) proved the concept of thin-shell capsules as a symmetry diagnostic for the NIF. Furthermore, the variation in symmetry with beam cone pointing shows that one-way capsule asymmetries could be corrected at the NIF. These quantitative results showed

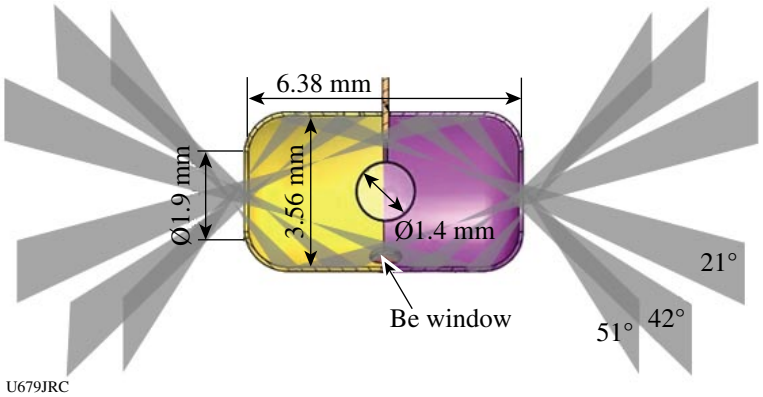

Figure 112.75
Gold hohlraum with an x-ray diagnostic port used in thin-shell symmetry capsule experiments. The capsule is a 1400-μm-diam, 15-μm-thick CH shell filled with 1 atm of D_2.

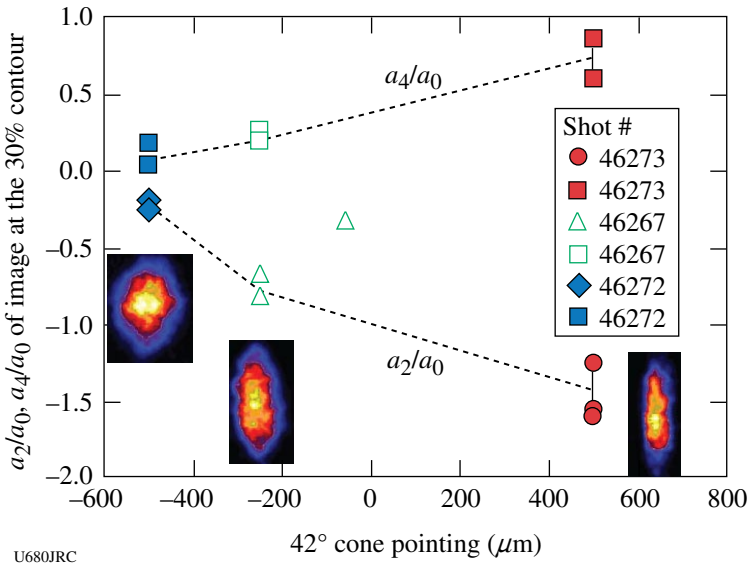

Figure 112.76
Observed time-integrated x-ray images and corresponding P_2 and P_4 asymmetries as the pointing of the 42° cone is moved along the hohlraum axis.

that we can now proceed to tune asymmetry in the foot of a full-scale NIF ignition capsule using the 96-beam configuration in FY08!

Convergent Ablator: Two shots days were dedicated to investigating the slowing of protons from the D + ^{3}He reaction to diagnose the ablator remaining at ignition in a NIF target in collaboration with MIT. Capsules were imploded in a 3/4-scale OMEGA hohlraum driven by 19 kJ in a 1-ns square pulse with hohlraum temperatures peaking at ~270 eV. By driving different thicknesses of CH capsules we could obtain different final ablator and fuel ρR's to test our ability to observe and calculate downshifts of the 14.7-MeV proton by up to ~1.5 MeV.

The results of this campaign confirmed our predictions of hohlraum temperature and our ability to observe gated images in self-emission of the imploding capsules. Figure 112.77 shows the observed neutron yields from nine capsules for capsule wall thicknesses varying from 25 to 55 μm thick. The points labeled "Nom 70% LEH" are calculated yields without mix. The triangles include expected degradation by mix as the capsules converge more with increasing initial thickness. Observed x-ray images for all but the 55-μm-thick capsules were round. MIT is now analyzing the charged-particle detectors to obtain total proton yield and spectra from emitted protons. Initial results with a 35-μm-thick capsule had enough yield to obtain a spectra, and calculations agreed with the measured energy shift.

In a similar experiment,[26] abundant hard x rays were measured indicative of hot-electron production. By varying laser energy in each of the three laser cones, we were able to determine that hard x rays were being produced almost entirely by the innermost cone, and that hot-electron temperatures were >100 keV. The particle temporal diagnostic (PTD) and neutron temporal diagnostic (NTD) instruments, modified to become hard x-ray detectors, showed peak emission at ~0.7 ns and a subsequent decrease, within the 1-ns laser pulse. In calculations this corresponded to the appearance of a quarter-critical-density surface between hohlraum wall and capsule ablator expansions. We showed increased x-ray production when the plastic-capsule ablator was changed to beryllium from CH, and no 3/2ω radiation from either type. These results are still being analyzed but

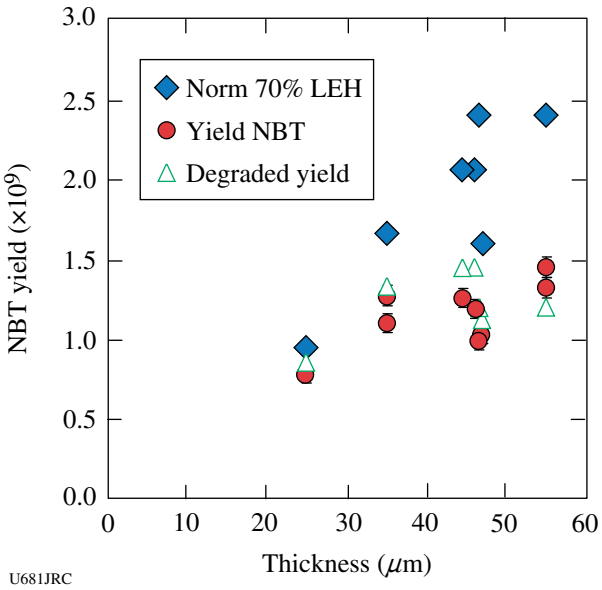

Figure 112.77
Observed and calculated D + D neutron yields from the convergent ablator experiment.

suggest that Raman scattering plays an important role in hot-electron production, as suggested from laser-instability postprocessing of the *LASNEX* hohlraum calculations.

Laser–Plasma Interactions: Gas-filled hohlraums are often used for high-energy-density laser experiments including inertial confinement fusion. While the gas fill is needed to provide a hot ionized plasma whose pressure prevents the ablated wall material from filling the hohlraum, it can also potentially lead to large laser–plasma instability growth since a long-scale-length quasi-homogeneous plasma is often created. One instability that may be detrimental to gas-filled hohlraum experiments is stimulated Raman scattering (SRS), which occurs when intense laser light resonantly decays into an electron-plasma wave and a backscattered light wave. Two strategies for mitigating SRS were investigated in FY07 on the OMEGA laser using gas-filled hohlraums.

The first strategy uses a small amount of a high-Z dopant in the low-Z gas fill, which had previously been observed to reduce SRS in experiments at the Helen laser and last year on the OMEGA laser. These experiments, which were a continuation of experiments started in FY06, heated a 1.6-mm-diam, 2.0-mm-length, Au gas-filled hohlraum. The hohlraum is filled with ~1-atm C_5H_{12} gas and has 0.25-μm-thick polyimide windows over the 0.8-mm-diam laser entrance holes (LEH's). The target is aligned along the B30 axis and heated with up to 12 kJ using 32 beams in three cones in a 1-ns pulse. After plasma formation, B30 is used to interact with the long-scale-length plasma with an intensity ~10^{15} W/cm^2, smoothed with a 150-μm CPP and full-bandwidth SSD. The 3ω transmitted-beam diagnostic (TBD) measures the transmitted light, and the full-aperture backscatter station (FABS) measures SRS and SBS growth. For this set of experiments, a small amount of Xe dopant was added to the gas fill and systematically varied up to 9% atomic fraction. These experiments indicate greater than a factor-of-2 decrease in SRS reflectivity when the Xe dopant is 1%. Experiments with a B30 intensity of 1.8×10^{15} W/cm^2 with SSD on or at 10^{15} W/cm^2 with SSD off show little change in SRS with 1% Xe. Comparison of these results with radiation hydrodynamic calculations is ongoing and will help rule out whether the effect can be simply explained by an increase in inverse Bremsstrahlung absorption, or whether competition of SRS with beam spray is the mechanism responsible for the observed decrease in SRS.

The second strategy examined this year used lower-density gas fills to increase Landau damping via the dimensionless parameter $k\lambda_D$, where k is the wave number and λ_D is the Debye wavelength. To examine the effects of high-$k\lambda_D$ regimes on SRS, the critical onset intensity for SRS is measured. A critical onset occurs theoretically for a random-phase-plate–smoothed laser beam with a distribution of intensities with a well-defined spatial correlation length (speckle length). As the average laser intensity increases, the calculated SRS gain diverges, leading to a saturated reflectivity. This is experimentally determined by measuring a sharp increase from no reflectivity to large reflectivity for a small increase in laser intensity. As $k\lambda_D$ increases, Landau damping of the electron-plasma wave increases, thus increasing the SRS critical onset intensity. In these experiments, mixtures of C_5H_{12} and C_3H_8 were used at different pressures to vary the electron density. B30 was used at an intensity of 10^{15} W/cm^2 with SSD to interact with the preformed hohlraum plasma and drive SRS. As the electron density is lowered, the critical onset for SRS occurs at a higher intensity, qualitatively consistent with theory. In Fig. 112.78, the presence of large SRS (>10%) is plotted in the gray circles, and the presence of small SRS (<1%) is plotted as open circles. For a small change in plasma density at a fixed laser intensity, or a small change in laser intensity at a fixed plasma density, SRS increases rapidly to a saturated state. The dashed line is plotted as a guide to indicate the demarcation of the measured critical onset.

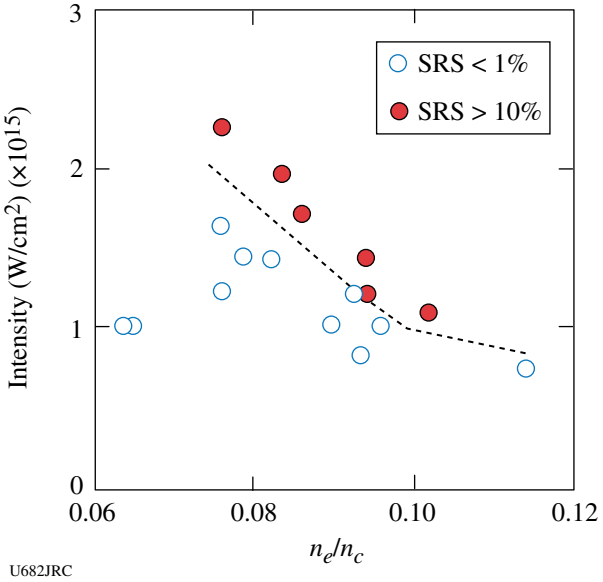

Figure 112.78
SRS levels as a function of n_e/n_c. The dashed line is plotted as a guide to indicate the demarcation of the measured critical onset.

Hi-Z: To better understand the effects of instability growth and the resulting mix, we need to be able to calculate the performance of capsule implosions with known quantities of

preimposed mix. Two days of directly driven implosions on the OMEGA laser in 2007 have tested the effects of pre-mix of Ar, Kr, and Xe in D_2 + ^{3}He–filled glass microballoons. In FY07 we focused on the effects of argon pre-mix, while earlier experiments explored Kr and Xe. Diagnostics included D + D and D + T neutron yields, D + ^{3}He proton yields and spectra, Doppler-broadened ion temperatures, time-dependent neutron and proton burn rates, and time-gated, high-energy filtered x-ray images. Simulated yields agree better with the experiment when calculated by XSN LTE[27] than by non-LTE atomic physics packages.

Measured yields with a small amount of pre-mix, atom fractions of ~5×10^{-3} for Ar, 2×10^{-3} for Kr, and 5×10^{-4} for Xe are more degraded than calculated, while the measured ion temperatures are the same as without pre-mix. There is also a decrease in fuel ρR. The neutron burn histories suggest that the early yield coming before the reflected shock strikes the incoming shell is undegraded, with yield degradation occurring afterward. Adding 20%-by-atom ^{3}He to pure-D fuel seems to produce a similar degradation. This ^{3}He degradation was previously observed in directly driven plastic shells by Rygg *et al.*[28] Figure 112.79 shows how calculated gated x-ray images agree in radius with the observed images when the reflected shock strikes the incoming shell at 1.18 ns but are smaller than the observed images afterward. This lack of convergence and lower fuel density partially explains the yield degradation as well as the low fuel and whole capsule ρR's observed in secondary T + D neutrons and slowing of the D + ^{3}He protons. Neither the LTE nor non-LTE models capture the degradation by ^{3}He or with low Ar, Kr, and Xe pre-mix levels, nor do they match the large shell radii after impact of the reflected shocks.[29]

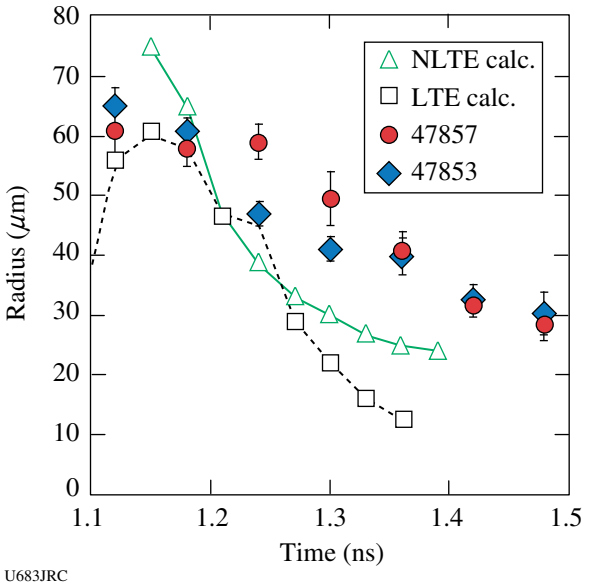

Figure 112.79
X-ray-image radius with (shot 47857) and without (shot 47863) ^{3}He versus simulated using LTE and non-LTE.

Reaction History: In October 2006, LANL conducted the *Reaction History Structure Using a Double Laser Pulse* experiment to study the effects of time-dependent mix in a DT capsule implosion. Two temporally separated laser pulses, as seen in Fig. 112.80(a), were used to obtain double peaks in the fusion reaction history as determined by deconvolved measurements from the gamma-based gas Cherenkov detector (GCD) and the

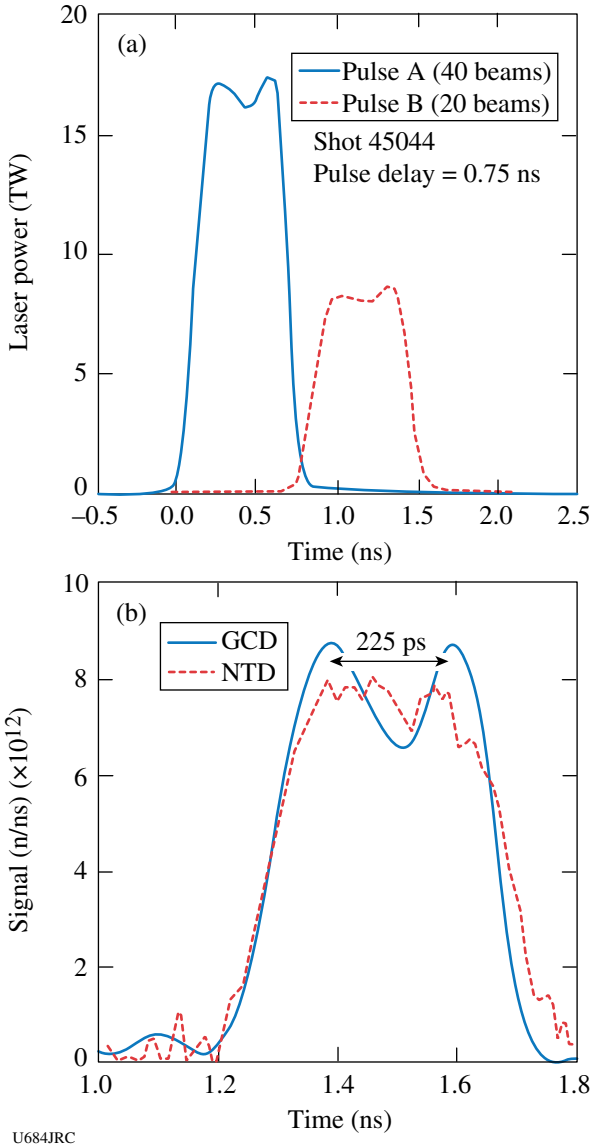

Figure 112.80
(a) Double-pulse laser waveforms; (b) double-pulse reaction history.

neutron temporal diagnostic (NTD) as shown in Fig. 112.80(b). The expected double-peak character of the reaction history is well resolved by the GCD. The first laser pulse contained 10 kJ in 40 beams and the second 5 kJ in 20 beams. Each was a square 600-ps pulse. This shorter-than-usual 1-ns laser pulse allows the shock and compression fusion burn components to be separated in time. Comparisons with modeling are indicating that the first peak is dominated by shock yield and the second peak, a result of compression burn, becomes significant only when the delays between pulses are less than 800 ps. This is contrary to the leading mix models, such as Scannapieco and Cheng, which predict a dominant compression burn, and is requiring us to invoke the harsh mix of a fall-line mix model to explain these observations.

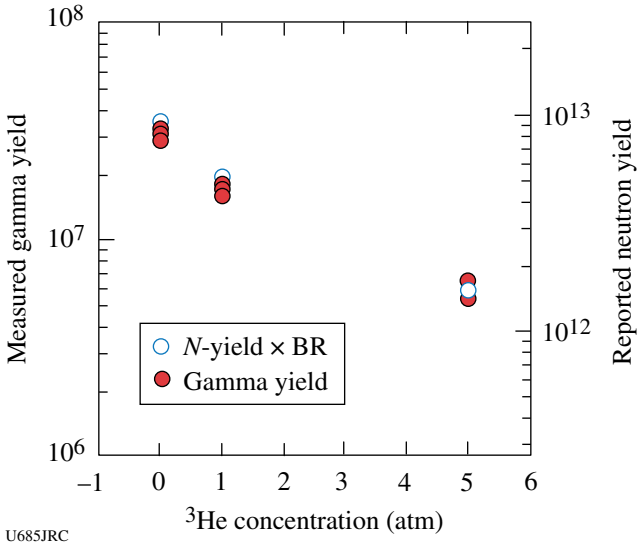

Figure 112.81
Neutron and γ-ray yields versus ^{3}He concentration shows a decrease in yield as the ^{3}He concentration is increased.

DTRat: In June 2007, LANL conducted the *DT Ratio-^{3}He Addition (DTRat)* experiment to investigate the effect of ^{3}He on the yield and reaction history of DT implosions. The DTRat experiment also used 600-ps laser pulses, but at 50% more energy: 15 kJ versus 10 kJ in the first pulse of the double-pulse experiment. As seen in Fig. 112.81, the absolute DT fusion gamma and neutron yields are consistent with each other and dropped by 80% in going from 0% to 33% ^{3}He addition (i.e., 5 atm ^{3}He). The shock and compression burns agree with the Scannapieco and Cheng mix model relatively well as determined by the GCD-measured reaction history shown in Fig. 112.82, so there was no need to resort to fall-line mix in this case. In both calculations and experiment, the compression burn is clearly much more degraded by the addition of ^{3}He than is shock burn.

The MIT group had previously determined that the addition of ^{3}He to DD in thick plastic shells resulted in approximately a factor-of-2 anomalous drop in scaled yield [i.e., yield over clean (YOC)] at 50% ^{3}He by atom as compared to pure DD or nearly pure ^{3}He, as seen in Fig. 112.83 (Ref. 27). While a drop in scaled yield with the addition of ^{3}He was observed for DT, it was not

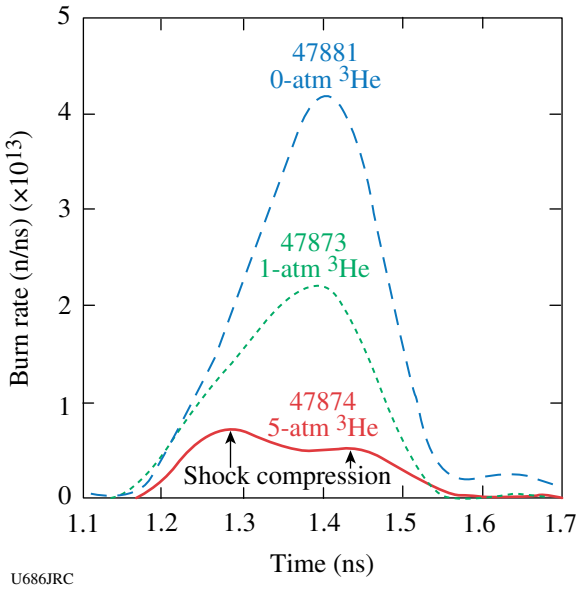

Figure 112.82
Burn history versus ^{3}He concentration.

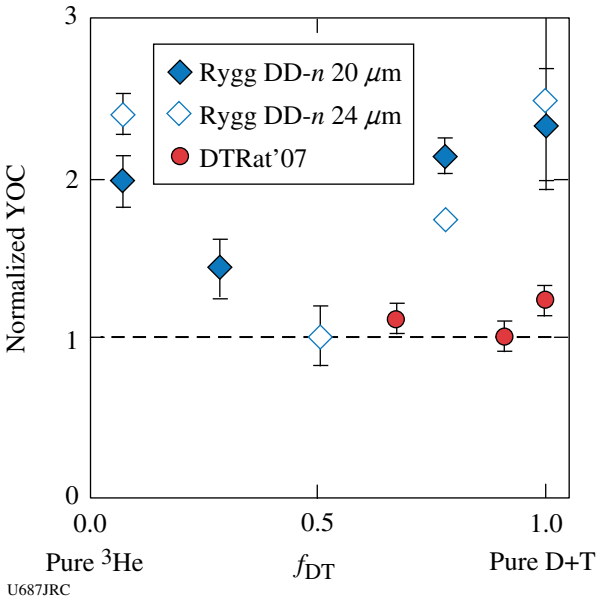

Figure 112.83
Scaled neutron yield normalized to 1 at the minimum for 20- and 24-μm plastic shells (Rygg) and 4.7-μm glass shells (DTRat'07).

nearly as significant as reported for DD. These data are the first of a planned series to study the effects of ^{3}He concentration on implosion yield and reaction history using DT capsules.

Beta Mix: Ignition experiments at megajoule/terawatt laser facilities will take the field of high-energy-density science into new frontiers, in terms of both physics and diagnostic capabilities. In particular, understanding the nature and amount of mix caused by hydrodynamic instabilities in inertial confinement fusion (ICF) targets is important from a fundamental physics perspective as well as for optimizing target performance. A radiochemical diagnostic to measure the amount of mix is being developed at Los Alamos National Laboratory. Figure 112.84 shows a conceptual diagram of how the diagnostic would be implemented. Neutrons produced in deuterium and tritium fusion interactions traverse the fuel to the ablator interface where they can upscatter tritons to MeV energies. Given the electron density or temperature (T_e) in this region, the triton range is quite short. Thus, the probability for ^{9}Be(t,x) interactions will depend strongly on the amount of mix that has occurred.

The diagnostic proposed for the National Ignition Facility is to collect and measure ^{8}Li atoms produced in ^{9}Be(t,α) interactions. Short-lived radiochemical signatures, such as ^{8}Li (half-life of 840 ms, and a Q_β of 13.4 MeV), provide a distinguishable signature for measuring mix, as MeV-scale backgrounds from prompt activation at the millisecond and greater timescales should be small. Further, this approach is not subject to systematic uncertainties from nontarget backgrounds from which stable and metastable isotope techniques can suffer. The two keys to executing this diagnostic are the ability to collect target debris after the implosion and the ability to begin counting the radionuclide decays of interest within this collected debris.

To gain insight into the issues surrounding radionuclide counting after a high-yield ICF shot, experiments were performed on OMEGA. Detectors were located both on the target chamber wall and inside a re-entrant tube to provide a prompt, high-fluence flash of radiation that must be addressed prior to initiating counting. The prompt radiation burst was also used as an activation source for counting experiments. Activation targets were located directly in front of the counters and included graphite and ^{15}N-enriched NH_4Cl. The graphite provided a source of ^{12}B atoms ($\tau_{1/2}$ = 20.2 ms, Q_β = 13.4 MeV) through ^{12}C(n,p)^{12}B interactions, while the ammonium chloride was a source of ^{15}C atoms ($\tau_{1/2}$ = 2.45 ms, Q_β = 4.5 and 9.8 MeV) through ^{15}N(n,p)^{15}C interactions. Figure 112.85 shows the results of measurements made with the graphite target. The data were collected using a scintillation telescope, with a Pilot-B scintillator and Burle 8575 photomultiplier tubes (PMT's). The PMT bases were custom bases that included a gating circuit to reverse bias the photocathode of the PMT to partially blind the tube during the prompt radiation burst. The anode signals from each PMT were discriminated, subjected to a coincidence requirement, and recorded in a multchannel scaler. The scaler data were then fit in the region of the ^{12}B decay, and an abundance calculation was made. From this abundance measurement, and a Geant 4 simulation to estimate efficiency and acceptance, it is possible to make a preliminary ^{12}C(n,p)^{12}B cross-section measurement of 300±30 μb at 14.1 MeV.

Debris collection appears to be the most challenging of the two key issues for this diagnostic. A number of attempts have been made to collect target debris at various laser facilities around the world, including OMEGA, but with mixed results. Although gas-collection schemes appear to have been successful, they are not practicable for short half-life counting diagnostics. Figure 112.86 illustrates why it is challenging to

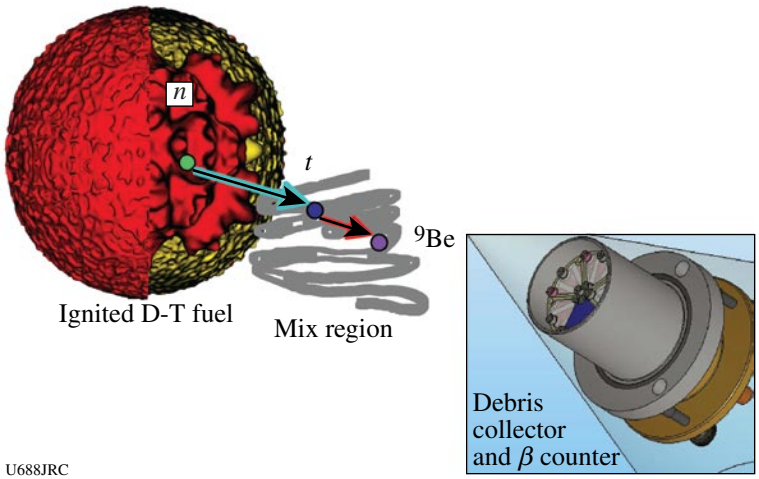

Figure 112.84
Illustration of the "beta-mix" diagnostic concept. Fast neutrons upscatter tritons in the fuel–ablator mix region. Triton–ablator reactions produce unstable daughters with millisecond to second half-lives that are collected and counted by a distant detector.

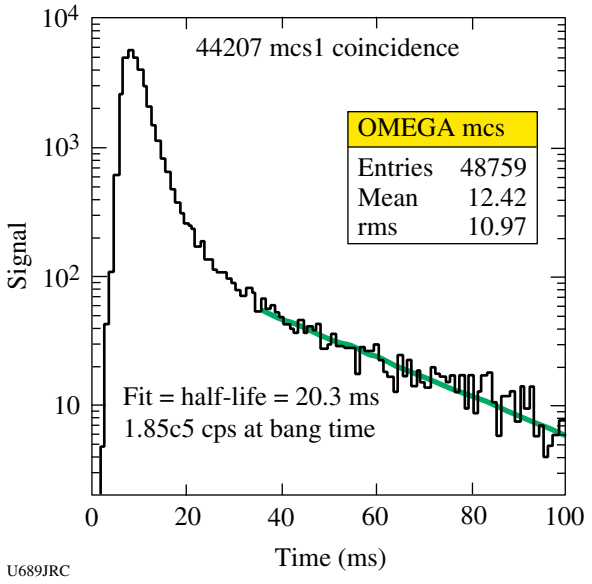

Figure 112.85
Counting data from a Pilot-B coincidence telescope. The half-life fit to the data is consistent with ^{12}B, and the resulting abundance is used to calculate a $^{12}C(n,p)^{12}B$ cross section of 14.1 MeV of 300±30 μb.

collect solid debris on direct-drive experiments. In an effort to improve efficiency of collection within a diagnostic cone, it is desirable to place collector materials as close to the target as possible. Unfortunately, in yield-producing direct-drive shots, two precursor shock waves strike the collector prior to the debris of interest. The first shock is due to the x rays produced at maximum compression. The second, and more damaging, shock in direct-drive scenarios is produced by the ions ablated from the target during laser illumination. The ions are calculated to have ~40 keV of kinetic energy, and if the collector is located close enough to the target, the energy density delivered to the surface of the collector is sufficient to eject a significant amount of mass from this collector. This ejected material drifts with velocities in the cm/μs range normal to the surface. Ejecta formation is illustrated in Fig. 112.87, which shows the surface profile of a 0.004-in. Ti collector foil that was exposed to three direct-drive shots. The foil was positioned 15 cm from the targets and partially covered. Approximately 160 nm of Ti foil was removed from the exposed portion of the foil on each shot. Disassembled target material, which would carry the mix signal of interest in putative experiments, follows the precursor shock materials with kinetic energies calculated to be ~10 keV. Stopping calculations estimate the mean implantation depth of the ~10-keV ions in room-temperature, solid-density Ti is of the order of ~20 nm, which is eight times less than the thickness of material removed by the ablated material shock. These dynamics may explain why past solid collection schemes have met with marginal success.

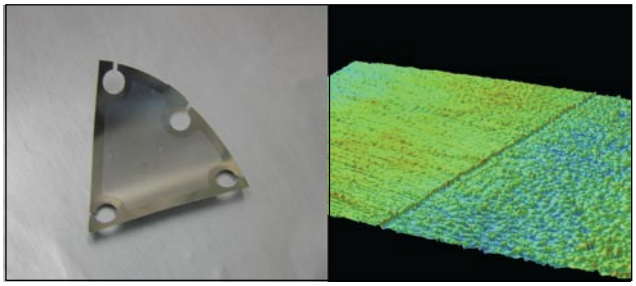

Figure 112.87
A Ti debris-collector foil exposed to three direct-drive shots of CH shells filled with 5 atm of D_2. The right panel shows the difference between exposed and unexposed surfaces. Approximately 160 nm of material was removed on each shot.

During the past year, both counting detector optimization and debris collection experiments have been performed on OMEGA, in support of the Mix in Inertial Confinement Fusion, LDRD DR at Los Alamos National Laboratory. The experi-

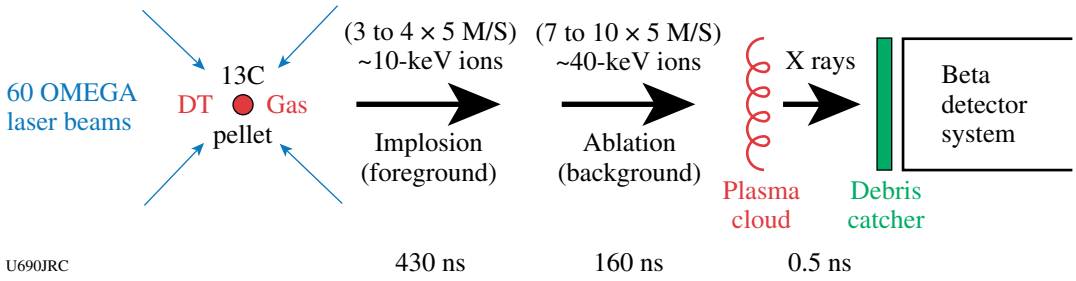

Figure 112.86
Illustration of the shock fronts impinging a debris collector in direct-drive ICF implosions. For a mix diagnostic, the signal is carried in the third shock front to strike the collector.

ments have shown that it is straightforward to count millisecond half-life decays of radionuclides following high-yield implosions on OMEGA. Further, studies are underway to optimize the performance of the counting scheme and to understand the issues to implement such a system in an environment appropriate for megajoule/terawatt-class laser facilities. Debris collection studies have also been initiated. The dynamics of solid debris collection are beginning to be understood, and work during FY08 will be focused on furthering understanding of the dynamics and implementing mitigation strategies to optimize the collector efficiency.

FY07 Sandia National Laboratories
OMEGA Experimental Programs

HDC Ablation-Rate Measurements in Planar Geometry: Accurate knowledge of the x-ray ablation rates of low-*Z* capsule materials will be essential for successful indirect-drive ICF ignition experiments. As part of the U.S. National Ignition Campaign, we have over the past few years performed experiments to measure the x-ray ablation rates in beryllium, copper-doped beryllium, polystyrene (CH), germanium-doped CH, and polyimide. In FY07, we performed the first measurements of the x-ray ablation rates of the diamond-like high-density-carbon (HDC) ablator that has been proposed as a NIF ignition capsule material.[30] The experimental technique for ablation-rate measurements in planar geometry is illustrated in Fig. 112.88 (details in Ref. 31). Basically, ablator samples are placed over an opening on the end of a halfraum. Laser beams that enter through the LEH provide the input power required to maintain the radiation field. The Dante array of K- and L-edge filtered photocathodes views the hohlraum wall through the LEH, and a time- and spectrally resolved measurement of the hohlraum radiation field is obtained from this data. An x-ray framing camera views the interior surface of the ablator sample, and the relative x-ray re-emission of the ablator versus the Au wall is determined. The streaked x-ray imager (SXI) diagnostic views the exterior surface of the ablator sample. The SXI employs an imaging slit, a transmission grating, an offset slit, and a streak camera to provide a highly time-resolved streaked image of the x-ray burnthrough flux on the exterior-facing side of the sample (as shown in Fig. 112.88). The combined information from these three measurements over a series of experiments is used to determine the mass ablation rate

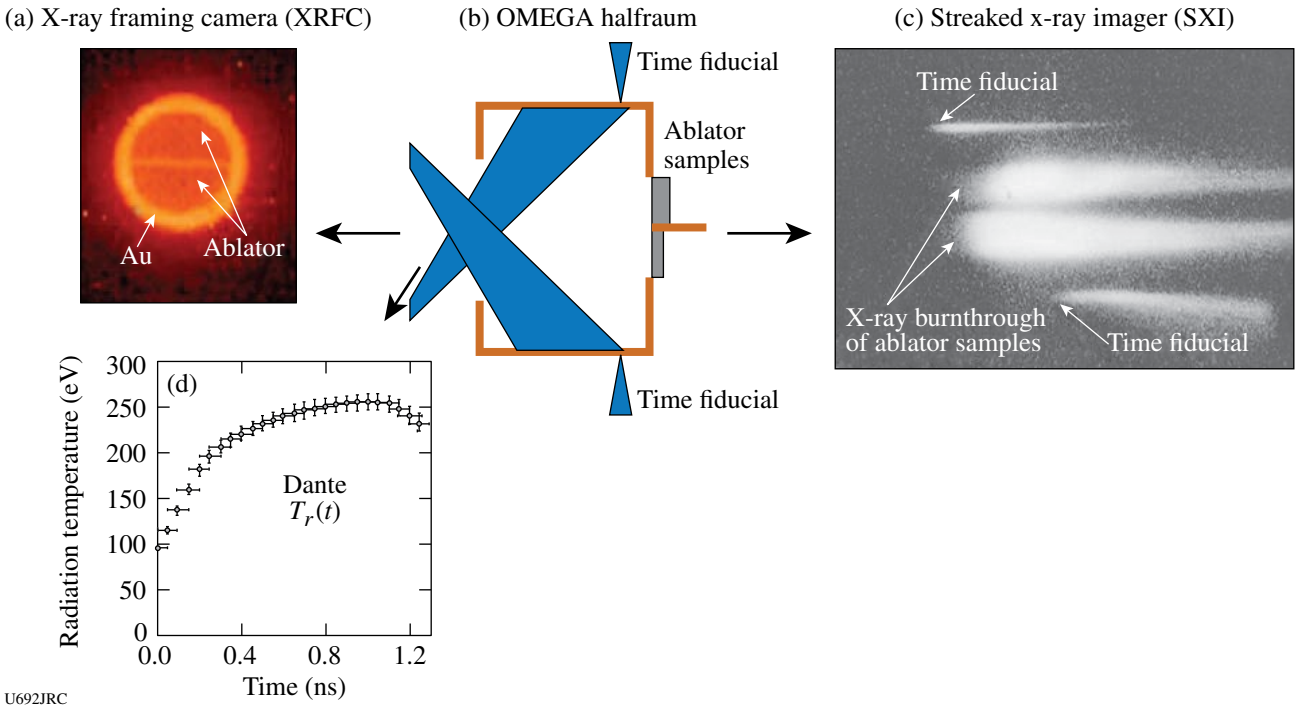

Figure 112.88
(a) The x-ray framing camera (XRFC) provides an x-ray re-emission flux relative to the re-emission of the Au wall (and, therefore, an estimate of the absorbed x-ray flux). (b) Schematic of the burnthrough experiment. (c) The streaked x-ray imager (SXI) measures burnthrough time for each ablator sample thickness. (d) The Dante diagnostic provides a time-resolved hohlraum radiation temperature.

(mg/cm^2/ns) as a function of hohlraum radiation temperature. In previous work, we found that the ablation rates in beryllium range from about 3 to 12 mg/cm^2/ns for hohlraum radiation temperatures in the range of 160 to 250 eV [Fig. 112.89(a)]. As expected, the HDC ablation rates are a bit lower, in the range of 2 to 9 mg/cm^2/ns for temperatures in the range of 170 to 260 eV [Fig. 112.89(b)]. The corresponding implied ablation pressures are in the range of 40 to 160 Mbar for beryllium and 20 to 140 Mbar for diamond (Fig. 112.90). Our post-shot computational simulations (shown as squares

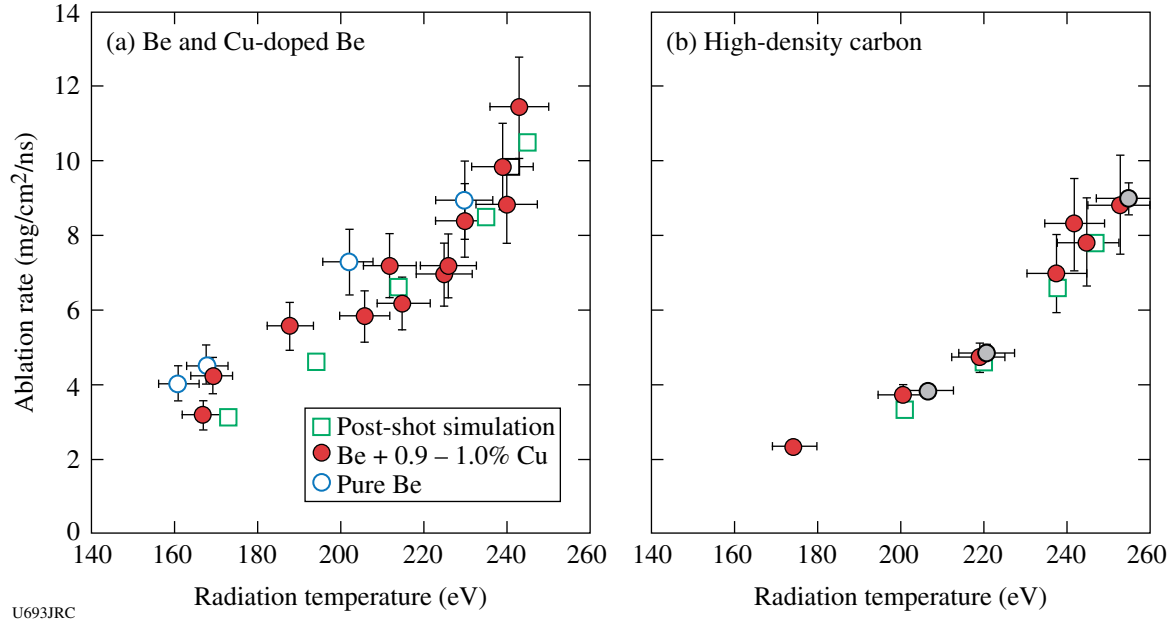

Figure 112.89
Ablation rates measured for radiation temperatures in the range of 160 to 260 eV for (a) Be and Cu-doped Be and (b) high-density carbon.

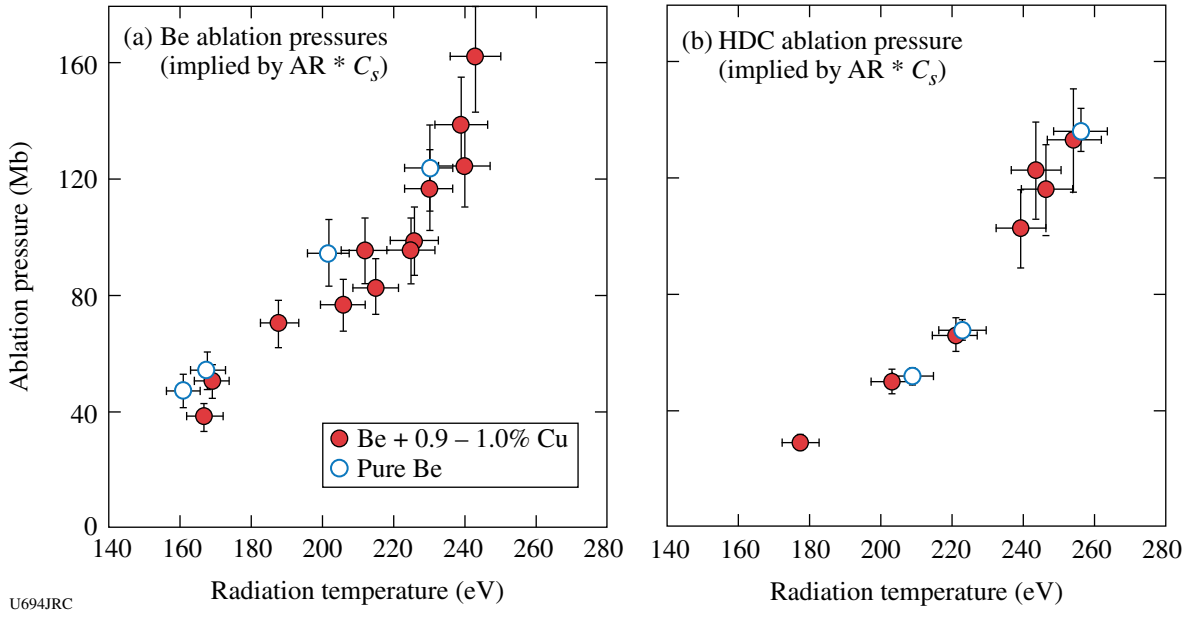

Figure 112.90
Corresponding ablation pressures implied by the data of Fig. 112.89. The Be and HDC ablators approximately follow a $P_r \sim T^{3.5}$ scaling.

on the Fig. 112.89 plots) are mostly within the uncertainties of the ablation-rate measurements. An iterative rocket model has been developed and used to relate the planar ablation-rate data to convergent OMEGA ablation-rate experiments and also to full-scale NIF ignition capsule calculations.

FY07 CEA OMEGA Experimental Programs

Wall-Motion Experiment: Measurements of wall and laser-spot motion in a cylindrical hohlraum were obtained on the OMEGA Laser Facility on 11 September 2007. Wall motion was measured using axial imagery with an x-ray framing camera (XRFC) in the axis of the hohlraum while laser-spot motion was measured using an x-ray streak camera (SSCA) looking through a thinned wall of the target (Fig. 112.91).

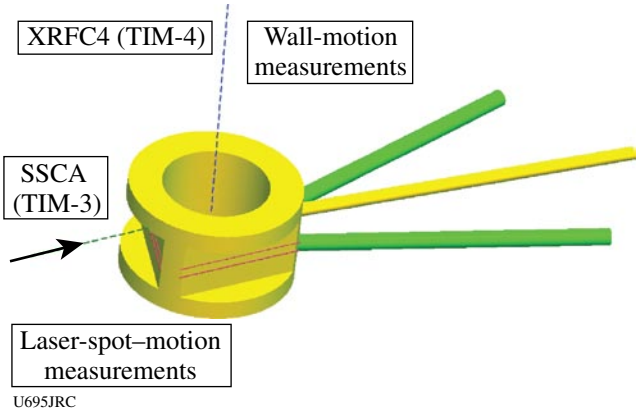

Figure 112.91
Schematic of experimental configuration for OMEGA wall-motion experiments.

Empty hohlraums, CH-lined hohlraums, and a propane-filled hohlraum were shot. Axial imagery (Fig. 112.92) shows that plasma striction comes early in empty hohlraums, while lined and gas-filled targets restrict wall expansion during the PS26 laser irradiation.

Streak images corroborate these results by showing a quicker expansion of laser spots in the case of an empty Au hohlraum (Fig. 112.93).

Neutron Imaging on OMEGA: In a directly driven implosion of a DT capsule, the CEA neutron-imaging[32] system uses a penumbral coded aperture to cast an image of the neutron source onto a detector. The system now routinely provides neutron images with 20-μm resolution. Recently, the system has been used for the first time ever during the implosion of a DT cryo target. An image of the DT cryo implosion is shown in Fig. 112.94(a); an image of a gas-filled target

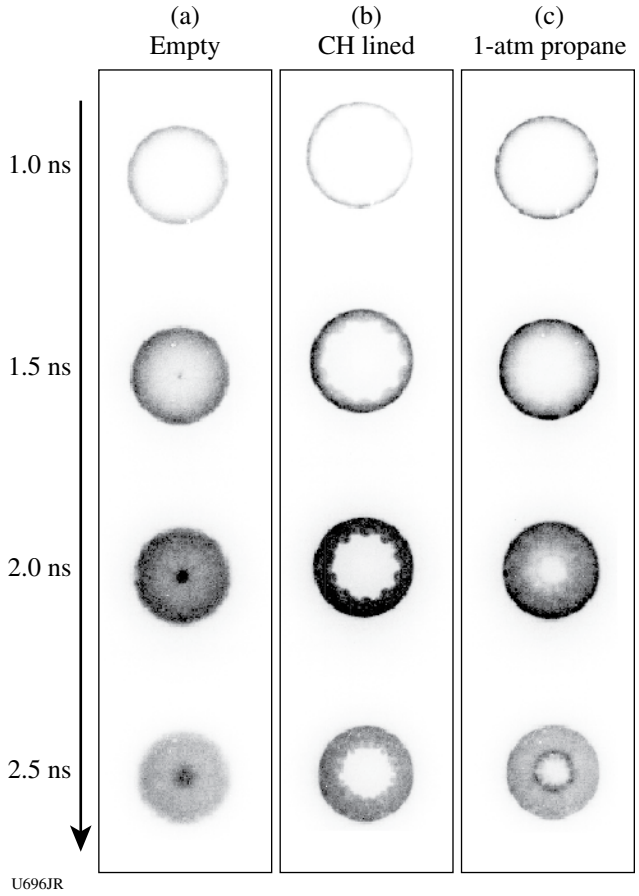

Figure 112.92
Axial x-ray framing camera images of wall motion in (a) empty, (b) CH-lined hohlraums, and (c) 1-atm-propane–filled, respectively.

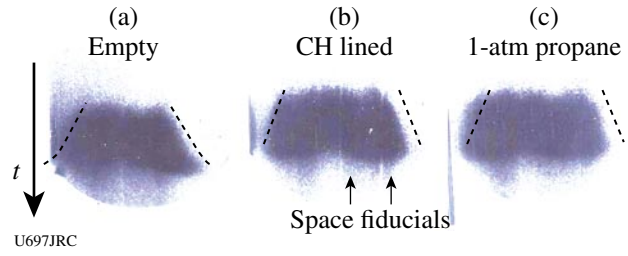

Figure 112.93
Spatially resolved streak-camera images of laser-spot motions in (a) empty, (b) CH-lined, and (c) propane-filled hohlraums.

imploded during the same shot day is shown in Fig. 112.94(b) for comparison.

On the diagnostic technique, the last step of development is to achieve a more valuable measurement with a 10-μm resolution at the source. Novel detectors made of capillaries filled with a liquid scintillator now reach a few-hundred-microns

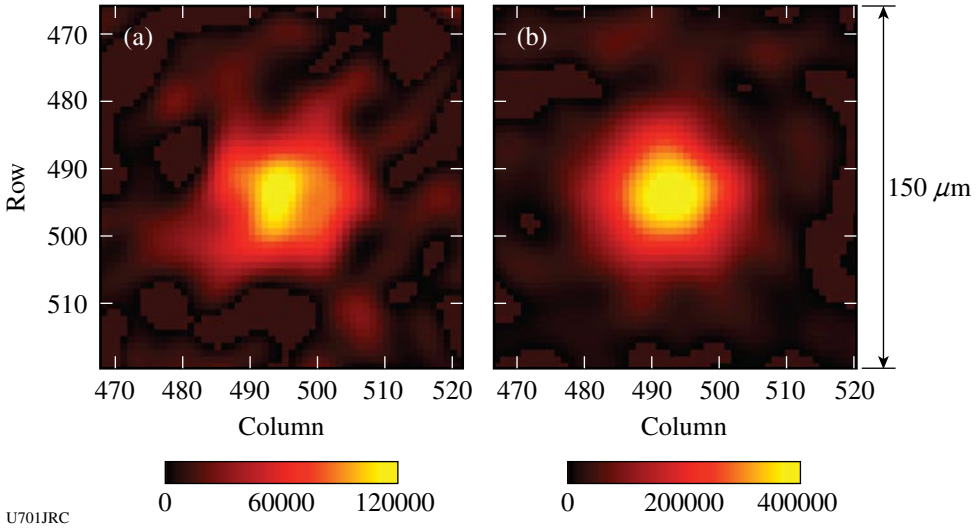

Figure 112.94
(a) Image of DT cryo implosion (shot 47575) yielding 1.1×10^{12} neutrons; (b) image of a DT(15)CH[15] implosion (shot 47551) producing 1.5×10^{13} neutrons.

spatial resolution, which moderates the required magnification ratio of the system and reduces the diagnostic line of path to a more practical distance (<30 m). A high-resolution diagnostic design now appears to be achievable but still requires addressing the resolution and the transmission across the field of view of the neutron aperture. As an example for the penumbral technique, a neutron point source transmitted through the aperture material casts a finite penumbra whose shape depends on the source location in the aperture field of view. This can result in an image distortion as classical unfolding methods assume a constant response across the field of view. These issues have been addressed this year both experimentally on OMEGA and with Monte Carlo calculations.

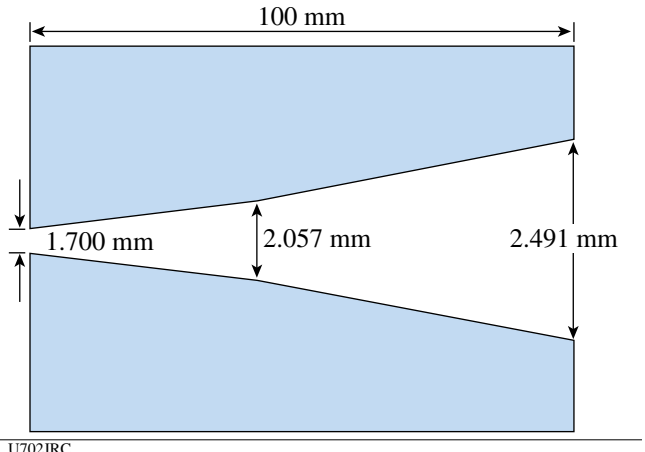

Figure 112.95
Penumbral aperture with a biconical shape made of tungsten.

Our work is performed with a penumbral aperture made by a pair of intersecting cones on the same axes (Fig. 112.95). The middle of the aperture is set at 260 mm from the target chamber center and has a ±100-μm field of view. Using the Monte Carlo code Geant 4, neutrons are transported through the biconical penumbral aperture. The neutron originates from a 50-μm-diam source, and penumbral images are generated for different locations of the source in the aperture field of view. Each of these images is unfolded using our standard autocorrelation method.[33] The reconstructed images present large distortions when the entire source is out of the field of view (see Fig. 112.96). However, when the source is at the edge of the field of view, there is clear distortion in the images.

Such distortions have also been investigated experimentally on OMEGA. The implosion of DT(15)CH[15] capsules produces an intense neutron source. Several neutron images using penumbral or annular apertures have shown a reproducible spherical source of 50-μm mean diameter. Therefore, the penumbral aperture was displaced between various shots performed with this target. The reconstructed sources are presented in Fig. 112.97 and agree with the conclusion deduced from the Geant 4 calculations. The ±100-μm field of view defined by the intersection of the two cones of the penumbral aperture appears to be very effective.

In the future, we plan to reproduce these experiments with a ring aperture as Monte Carlo calculations predict enhanced image distortion with the source position in the field of view.

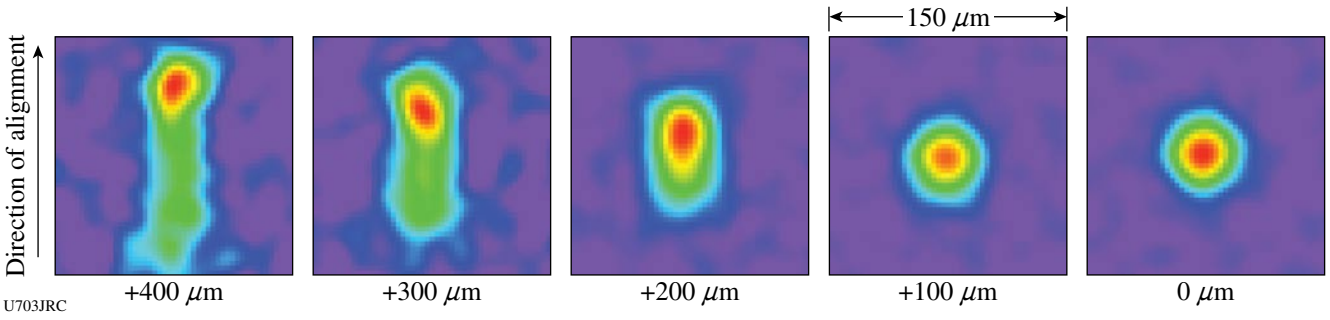

Figure 112.96
A 50-μm-diam neutron source at different locations in the field of view of a penumbral aperture using the Monte Carlo code Geant 4.

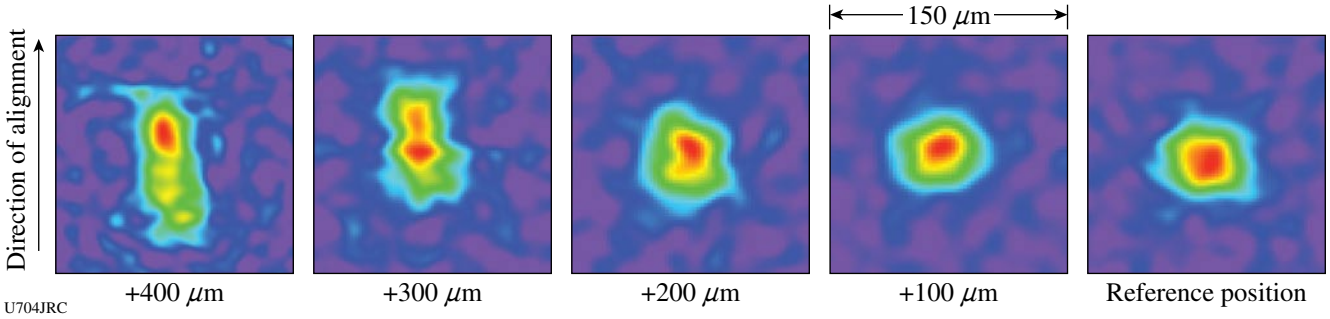

Figure 112.97
Experimental neutron images recorded at different positions in the field of view of a penumbral aperture. All images were recorded on a DT(15)CH[15] target implosion.

Also, the construction of a 150-mm-diam camera will allow us to record the image at a finer spatial resolution.

Neutron Flux and Duration Emission Measured with CVD Diamond Detectors: A series of chemical-vapor-deposition (CVD) diamond detectors have been implemented on OMEGA during a directly driven implosion of a DT capsule yielding 10^{13} to 10^{14} neutrons. These detectors discriminate neutrons by the time-of-flight technique and can provide a neutron-yield measurement after a calibration with the usual copper activation diagnostic. Neutron bang time and ion-temperature measurement can also be deduced from the probed signal as long as the diamond detectors exhibit temporal properties in the 100-ps range. Here the diamond devices used were grown and fabricated by CEA with controlled impurity levels (nitrogen, oxygen) that affect the sensitivity and the response time of the diamond detectors.[34] The relation between the level and nature of impurities with respect to the detector performances is, to date, empirical and has, therefore, required an experimental approach. These experiments have aimed at identifying the relevant characteristics of the diamond detectors to be suitable for neutron-yield, bang-time, and ion-temperature diagnostics.

Diamond detectors were inserted at distances of 30 cm, 1 m, and 2 m from the target chamber center using the TIM diagnostic insertion mechanisms. The distances and neutron-yield range provide the ability to probe the performances of the detectors within two decades of the neutron flux (n/cm^2). The detectors exhibit a linear response over the dynamic range explored. Sensitivity was also found reproducible on the A281103 diamond device tested in December 2005 and March 2007 (Fig. 112.98). Further, the diamond sensitivity can vary by a factor of 10^4 (Table 112.VII), which is mainly attributed to the material nature and the contribution of the added impurities since the geometrical dimensions of all detectors remained almost equal (3×3-mm^2 surface, 200 to 400 μm thick). Such results are essential to determine the required diamond detector characteristics as a function of location and detection volumes as NIF and LMJ experiments will require the neutron diagnostics to operate in the 10^{12} to 10^{18} neutron-yield range.[35]

The relative sensitivity between the diamonds as measured with the 14-MeV neutrons was also probed for comparison with 16-MeV electrons produced on a Linac accelerator at CEA (Bruyères le Châtel) (Fig. 112.99). A simple test on an electron

accelerator will make it possible to classify the diamond detectors prior to their installation on large ICF facilities.

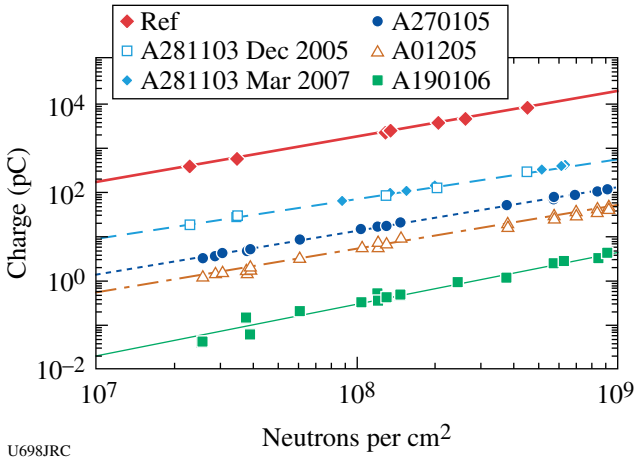

Figure 112.98
Linear response of a chemical-vapor-deposition (CVD) diamond measured on OMEGA.

The temporal properties of the detectors, such as rise time, FWHM, and decay time, were also measured from the short duration (25 ps) of the Linac electron pulses. Several diamond detectors show a 10% to 90% rise time below 100 ps and a subnanosecond decay time (Table 112.VIII). On OMEGA, the 150-ps-long neutron pulse makes it possible to measure the main temporal characteristics of the diamond detectors.

The detector signal propagates through 30 m of cable before reaching a 7-GHz-bandwidth single-shot oscilloscope (IN7100). After software removal of the dispersion caused by this cable, the diamond detector exhibits a signal duration at FWHM and a decay time comparable to those measured using the 16-MeV electrons. The signal rise time observed during DT implosions is, however, somewhat different since the neutron pulse duration at the detector position is determined by the 150-ps duration of the neutron source, convoluted with the temporal broadening induced by the DT ion's main energy at bang time. This ion-temperature effect is clearly observed on the signal rise time by probing the response at varying

Table 112.VII: Diamond sensitivity measured with a pulse of 14-MeV neutrons.

CVD	Type	Thickness	Size	Gold Contact	High Voltage	Sensitivity (C.n^{-1})
Ref	Monocrystalline	225 μm	4 × 4 mm	3 × 3 mm	–100 V	2.03×10^{-16}
A040406	Monocrystalline	260 μm	3 × 3 mm	2 × 2 mm	–750 V	4.15×10^{-18}
A281103	Polycrystalline	260 μm	5 × 5 mm	4 × 4 mm	–750 V	5.84×10^{-18}
A270105	Polycrystalline	250 μm	5 × 5 mm	4 × 4 mm	–750 V	1.06×10^{-18}
A010205	Polycrystalline	630 μm	5 × 5 mm	4 × 4 mm	–360 V	4.53×10^{-19}
A190106	Polycrystalline	450 μm	5 × 5 mm	4 × 4 mm	–500 V	2.70×10^{-20}

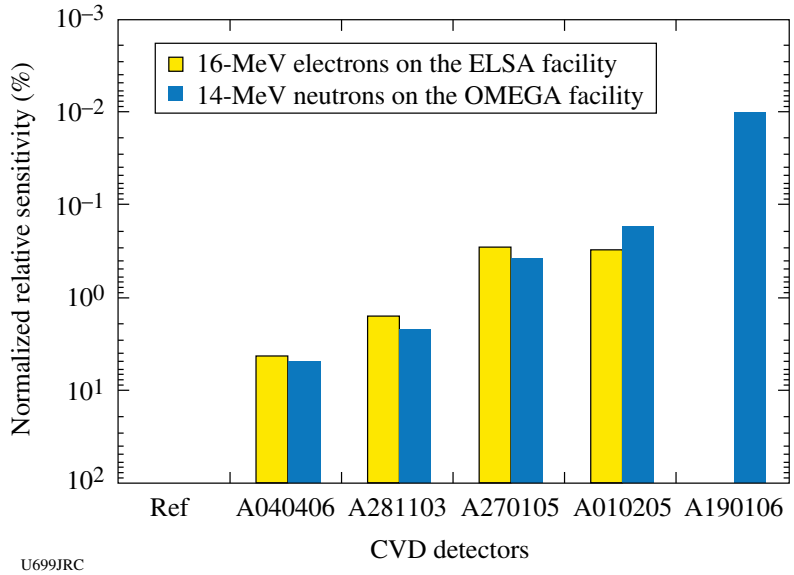

Figure 112.99
Comparison of electron and neutron relative sensitivity. All data are normalized by the most sensitive diamond "Ref."

Table 112.VIII: Temporal properties of diamond detectors as measured under 16-MeV electron pulses of 25-ps duration and 14-MeV neutron pulses of 150-ps duration.

CVD Detector	ELSA Facility 16-MeV Electrons			OMEGA Facility 14-MeV Neutrons		
	Rise (ps)	FWHM (ps)	Decay (ps)	Rise (ps)	FWHM (ps)	Decay (ps)
Ref	219	2870	4228	461	3508	4075
A040406	85	265	627	260	367	1340
A281103	134	434	772	226	442	688
A270105	73	297	608	164	318	601
A010205	86	178	540	133	241	322
A190106	n/a	n/a	n/a	150	266	917

distances—37 cm, 100 cm, or 200 cm—from the target (see Fig. 112.100—probed on the detector A270105).

Using the signal processing technique already used in the NTD diagnostics,[36] we deduce the neutron duration at 2 m from the target, which is mainly determined by the Doppler broadening produced by the ions. The resulting ion temperature and measured time duration are shown in the two last columns of Table 112.IX. For comparison, Table 112.IX also shows the ion temperature measured with the standard OMEGA system, performed at 5 m with a fast scintillator and an MCP photomultiplier. From these values, the time broadening (Δt) is deduced for a measurement at 2 m from target chamber center (TCC). The measured ion temperatures deduced from the CVD diamond at 2 m from the target are in good agreement with the standard OMEGA measurement.

A low-sensitivity CVD diamond with a high level of nitrogen impurity (A190106) demonstrates that diamond detectors can measure very high yield neutron for the NIF and LMJ. The

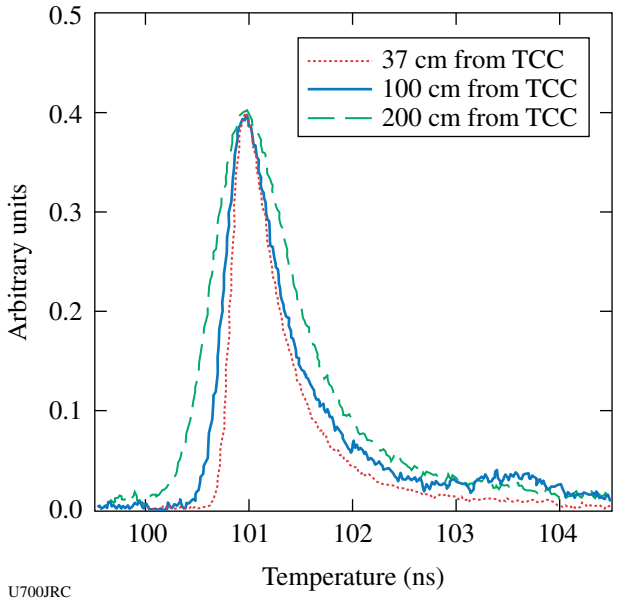

Figure 112.100
Doppler broadening of the neutron pulse.

Table 112.IX: Ion-temperature measurement at 2 m from TCC.

OMEGA Measurement			CVD Measurement		
N° Tir	T_i LLE (±0.5 keV)	Δt	CVD Reference	T_i Measured	Δt Measured
47539	3.4 keV	446 ps	A270105	3.8 keV	474 ps
			A010205	3.6 keV	456 ps
47540	3.6 keV	459 ps	A270105	3.5 keV	450 ps
			A010205	3.4 keV	449 ps
47549	5.4 keV	562 ps	A270105	5.5 keV	565 ps
			A010205	5.7 keV	576 ps
47550	5.1 keV	547 ps	A270105	5.0 keV	542 ps
			A010205	5.0 keV	542 ps

development of faster low-sensitivity CVD diamond detectors will continue with CEA-LIST and OMEGA. Ion-temperature measurement with CVD diamonds will be strengthened with future experiments.

One new challenging task will be to demonstrate the capability of a large, sensitive CVD diamond to measure the downscattered neutron yield for ρR determination.

FY07 AWE OMEGA Experimental Program

Radiation transport through enclosed spaces with inwardly moving walls is a key component of the physics of laser-heated hohlraums. It arises in the laser-heated cavity itself (where inward motion of the wall results in late-time stagnation of dense plasma on the hohlraum axis[37]) and also in the laser-entry and diagnostic holes (where an understanding of hole closure is important to hohlraum design and the interpretation of diagnostic data[38]). To better understand these phenomena, AWE (in collaboration with LLNL and General Atomics) successfully led two days of experiments on OMEGA during FY07.

A laser-heated hohlraum was used (Fig. 112.101) to illuminate annular slits machined in samples of solid-density tantalum and low-density, tantalum-oxide foam. In the first day of experiments (November 2006), the transmitted energy was measured indirectly (by measuring the temperature rise of a "calorimeter" hohlraum), directly (by measuring the emission from the tantalum-oxide component, using a target in which the calorimeter hohlraum was omitted), and by x-ray gated imaging of the slit. In the second series of experiments (May 2007), x-ray point-projection backlighting was used to determine the density distribution of plasma within a radiatively driven slit in solid-density tantalum. Figure 112.102 shows the measured temperature rise of the calorimeter hohlraum in comparison with radiation hydrocode simulation, for slits of two different widths and also for a sample of tantalum-oxide foam with no slit. Heating of the calorimeter arises from two sources: (1) x-ray transmission through the closing slit and (2) radiation burnthrough of the surrounding tantalum-oxide foam material. Both phenomena are modeled well by the simulation. Figure 112.103 shows point-projection radiographs of

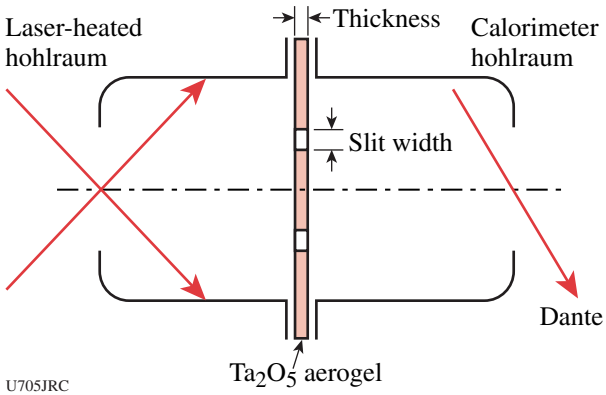

Figure 112.101
Schematic of the experiment to measure radiation transport through slits in low-density tantalum oxide and solid-density tantalum. One surface of the slit is heated by a scale-1.4 hohlraum target, and the transmitted energy either heats a "calorimeter" hohlraum or is measured directly (calorimeter not present). Radiographic measurements of the slit closure are made by point-projection backlighting along the hohlraum axis.

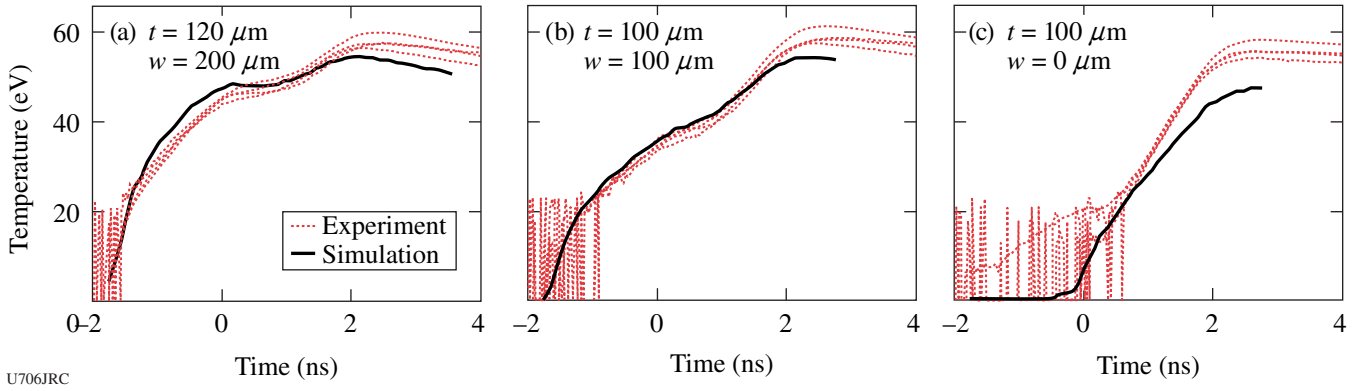

Figure 112.102
Temperature of the calorimeter hohlraum for experiments using low-density (0.25 g cm^{-3}) tantalum-oxide slits of (a) 120-μm thickness and 200-μm width, (b) 100-μm thickness and 100-μm width, and (c) 100-μm thickness with no slit. In each case the temperature inferred from four channels of the Dante diagnostic (a filtered x-ray diode array) is compared with simulation.

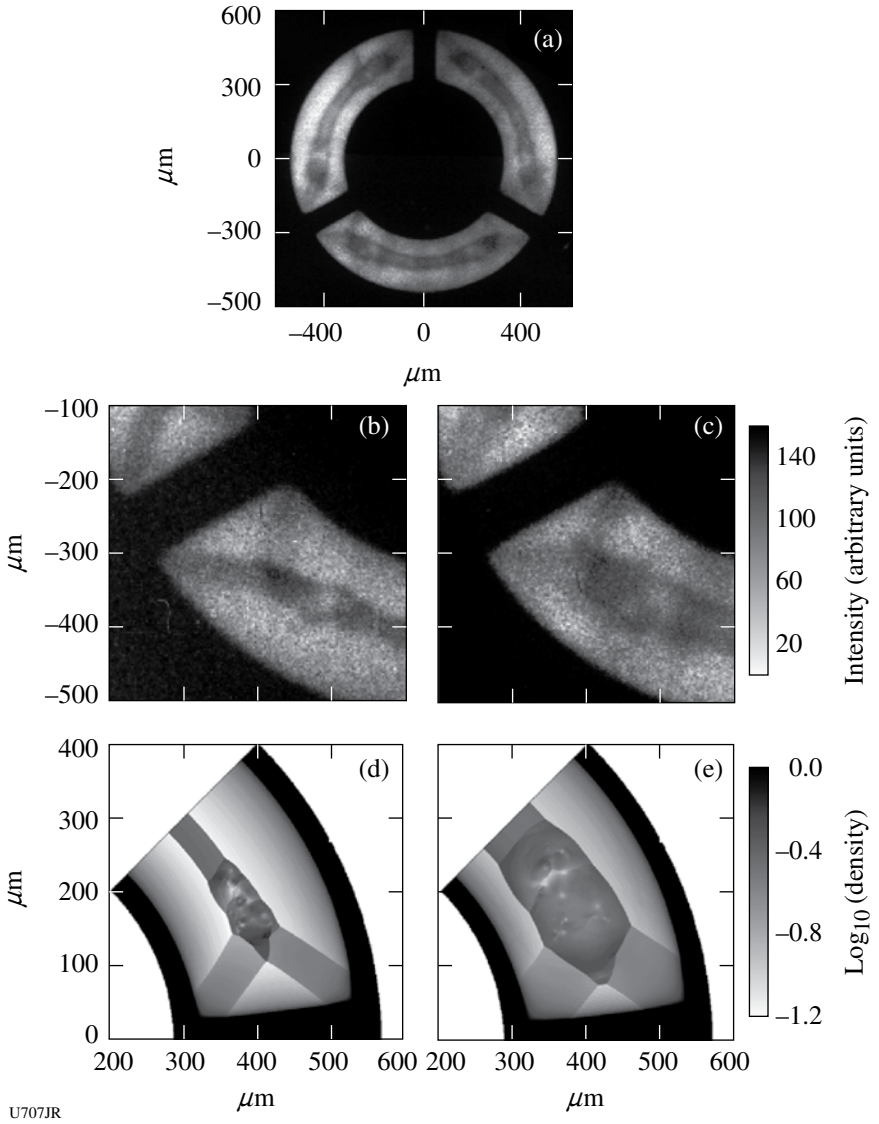

Figure 112.103
Point-projection radiographs of the closure of a 200-μm-wide slit in 50-μm-thick solid-density tantalum. (a) The deceleration shock and axial stagnation region within the slit are clearly visible. Images (b) and (c) are separated by 1.3 ns in time and show detail of the complex shock interactions in the corners bounded by the sides of the slit and the radial spokes supporting the central disk. Radiation hydrocode simulations (d) and (e) approximately reproduce this structure.

an annular slit in solid-density tantalum foil and comparison with a simulation in simplified (2-D Eulerian) geometry. The simulation approximately reproduces the deceleration shock and axial stagnation region at the center of the slit, as well as the complex shock interactions in the neighborhood of the radial spokes supporting the central disk. It is interesting to note that "N-wave" distributions of density, similar to the central stagnation region, also occur, in the astrophysical context, in stellar atmospheres[39,40] and that experiments of this type offer a potential laboratory platform for their investigation.

REFERENCES

1. S. Brygoo *et al.*, "Development of Quartz as an Impedance-Match Standard for Laser Shock Measurements in the Diamond Anvil Cell," submitted to the Journal of Applied Physics.

2. J. Eggert *et al.*, "Hugoniot Data for Helium in the Mbar Regime," to be published in Physical Review Letters.

3. G. W. Collins, Lawrence Livermore National Laboratory, private communication (2007).

4. D. Saumon and G. Chabrier, Phys. Rev. Lett. **62**, 2397 (1989).

5. S. A. Bonev, B. Militzer, and G. Galli, Phys. Rev. B **69**, 014101 (2004).
6. R. Jeanloz *et al*., Proc. Natl. Acad. Sci. USA **104**, 9172 (2007).
7. L. Stixrude and R. Jeanloz, "Fluid Helium at Conditions of Giant Planetary Interiors," submitted to the Proceedings of the National Academy of Sciences of the United States of America.
8. M. Ross, R. Boehler, and D. Errandonea, Phys. Rev. B **76**, 184117 (2007).
9. P. Celliers, Lawrence Livermore National Laboratory, private communication (2007).
10. J. M. Foster, B. H. Wilde, P. A. Rosen, R. J. R. Williams, B. E. Blue, R. F. Coker, R. P. Drake, A. Frank, P. A. Keiter, A. M. Khokhlov, J. P. Knauer, and T. S. Perry, Astrophys. J. Lett. **634**, L77 (2005).
11. R. F. Coker *et al*., Astrophys. Space Sci. **307**, 57 (2007).
12. C. K. Li, F. H. Séguin, J. A. Frenje, J. R. Rygg, R. D. Petrasso, R. P. J. Town, P. A. Amendt, S. P. Hatchett, O. L. Landen, A. J. Mackinnon, P. K. Patel, V. A. Smalyuk, T. C. Sangster, and J. P. Knauer, Phys. Rev. Lett. **97**, 135003 (2006).
13. C. K. Li, F. H. Séguin, J. A. Frenje, J. R. Rygg, R. D. Petrasso, R. P. J. Town, P. A. Amendt, S. P. Hatchett, O. L. Landen, A. J. Mackinnon, P. K. Patel, M. Tabak, J. P. Knauer, T. C. Sangster, and V. A. Smalyuk, Phys. Rev. Lett. **99**, 015001 (2007).
14. C. K. Li, F. H. Séguin, J. A. Frenje, J. R. Rygg, R. D. Petrasso, R. P. J. Town, O. L. Landen, J. P. Knauer, and V. A. Smalyuk, Phys. Rev. Lett. **99**, 055001 (2007).
15. C. K. Li, presented at the Fifth International Conference on Inertial Fusion Sciences and Applications, Kobe, Japan, 9–14 September 2007 (invited) (Paper ThO4.1).
16. R. Petrasso, Bull. Am. Phys. Soc. **52**, 97 (2007) (invited).
17. C. K. Li, F. H. Séguin, J. A. Frenje, J. R. Rygg, R. D. Petrasso, R. P. J. Town, P. A. Amendt, S. P. Hatchett, O. L. Landen, A. J. Mackinnon, P. K. Patel, V. Smalyuk, J. P. Knauer, T. C. Sangster, and C. Stoeckl, Rev. Sci. Instrum. **77**, 10E725 (2006).
18. J. F. Hansen, Lawrence Livermore National Laboratory, private communication (2007).
19. B. L. Henke *et al*., J. Opt. Soc. Am. B **1**, 818 (1984).
20. D. Vanderhaegen, J. Quant. Spectrosc. Radiat. Transf. **36**, 557 (1986).
21. G. C. Pomraning, J. Quant. Spectrosc. Radiat. Transf. **40**, 479 (1988).
22. G. C. Pomraning, *Linear Kinetic Theory and Particle Transport in Stochastic Mixtures*, Series on Advances in Mathematics for Applied Sciences, Vol. 7 (World Scientific, Singapore, 1991).
23. O. Haran, D. Shvarts, and R. Theiberger, Phys. Rev. E **61**, 6183 (2000).
24. C. C. Smith, J. Quant. Spectrosc. Radiat. Transf. **81**, 451 (2003).
25. P. D. Roberts *et al*., J. Phys. D: Appl. Phys. **13**, 1957 (1980).
26. P. Amendt *et al*., Bull. Am. Phys. Soc. **49**, 26 (2004).
27. W. A. Lokke and W. H. Grasberger, Lawrence Livermore National Laboratory, Livermore, CA, Report UCRL-52276, NTIS Order No. UCRL-52276 (1977).
28. J. R. Rygg, J. A. Frenje, C. K. Li, F. H. Séguin, R. D. Petrasso, J. A. Delettrez, V. Yu. Glebov, V. N. Goncharov, D. D. Meyerhofer, S. P. Regan, T. C. Sangster, and C. Stoeckl, Phys. Plasmas **13**, 052702 (2006).
29. D. C. Wilson *et al*., "The Effects of High Z Pre-Mix on Burn in ICF Capsules," submitted to the *Proceedings of the Fifth International Conference on Inertial Fusion Science and Applications (2007)* [to be published by Journal of Physics: Conference Series (Institute of Physics), London, England].
30. D. Ho *et al*., Bull. Am. Phys. Soc. **51**, 213 (2006).
31. R. E. Olson, R. J. Leeper, A. Nobile, J. A. Oertel, G. A. Chandler, K. Cochrane, S. C. Dropinski, S. Evans, S. W. Haan, J. L. Kaae, J. P. Knauer, K. Lash, L. P. Mix, A. Nikroo, G. A. Rochau, G. Rivera, C. Russell, D. Schroen, R. J. Sebring, D. L. Tanner, R. E. Turner, and R. J. Wallace, Phys. Plasmas **11**, 2778 (2003).
32. L. Disdier, A. Rouyer, I. Lantuéjoul, O. Landoas, J. L. Bourgade, T. C. Sangster, V. Yu. Glebov, and R. A. Lerche, Phys. Plasmas **13**, 056317 (2006).
33. A. Rouyer, Rev. Sci. Instrum. **74**, 1234 (2003).
34. P. Bergonzo, D. Tromson, and C. Mer, Semicond. Sci. Technol. **18**, S105 (2003).
35. V. Yu. Glebov, D. D. Meyerhofer, T. C. Sangster, C. Stoeckl, S. Roberts, C. A. Barrera, J. R. Celeste, C. J. Cerjan, L. S. Dauffy, D. C. Eder, R. L. Griffith, S. W. Haan, B. A. Hammel, S. P. Hatchett, N. Izumi, J. R. Kimbrough, J. A. Koch, O. L. Landen, R. A. Lerche, B. J. MacGowan, M. J. Moran, E. W. Ng, T. W. Phillips, P. M. Song, R. Tommasini, B. K. Young, S. E. Caldwell, G. P. Grim, S. C. Evans, J. M. Mack, T. Sedillo, M. D. Wilke, D. C. Wilson, C. S. Young, D. Casey, J. A. Frenje, C. K. Li, R. D. Petrasso, F. H. Séguin, J. L. Bourgade, L. Disdier, M. Houry, I. Lantuejoul, O. Landoas, G. A. Chandler, G. W. Cooper, R. J. Lepeer, R. E. Olson, C. L. Ruiz, M. A. Sweeney, S. P. Padalino, C. Horsfield, and B. A. Davis, Rev. Sci. Instrum. **77**, 10E715 (2006).
36. R. A. Lerche, D. W. Phillion, and G. L. Tietbohl, Rev. Sci. Instrum. **66**, 933 (1995).
37. R. T. Eagleton *et al*., Rev. Sci. Instrum. **68**, 834 (1997).
38. R. E. Chrien *et al*., Rev. Sci. Instrum. **70**, 557 (1999).
39. D. Mihalas and B. Weibel-Mihalas, *Foundations of Radiation Hydrodynamics* (Oxford University Press, New York, 1984).
40. T. K. Suzuki, Astrophys. J. **578**, 598 (2002).